

SPATIALLY RESOLVED LASER SCANNING FOR LARGE AREA
TESTING OF SILICON PHOTOMULTIPLIERS

CHLOE GINGRAS

Department of Physics
McGill University, Montreal

July 2023

A thesis submitted to McGill University in partial fulfillment of the
requirements for the degree of Master of Science

© Chloe Gingras 2023

To my father

Abstract

The discovery of nonzero neutrino mass forces us to confront the mechanism by which it arises. Current leading theories would have the neutrino be a Dirac particle, like all other fermions in the Standard Model, or a Majorana particle; the latter would provide a natural explanation for the smallness of neutrino mass. It would also require neutrinos to be their own antiparticles, and require lepton number violating processes beyond the Standard Model. A promising approach to search for Majorana neutrinos is via neutrinoless double beta decay, whose observation is the goal of the proposed nEXO experiment. nEXO's next-generation time projection chamber will contain 5 tonnes of liquid Xenon enriched to 90% in ^{136}Xe , an isotope known to undergo double beta decay. The energy and position of each event inside the detector will be reconstructed using ionization and scintillation signals. Silicon photomultipliers (SiPMs), $\sim 1\text{ cm}^2$ solid-state detectors with single photon resolution, have been chosen to detect the expected vacuum ultraviolet Xe scintillation light. nEXO plans to cover an area of 4.5 m^2 around the detector with SiPMs, requiring thousands of these devices. Testing the large number of SiPM modules at operating temperatures will require an automated approach and high throughput of SiPMs to be done in a reasonable timescale for nEXO. This thesis presents results from the commissioning of a precision scanning mechanism which has been developed to systematically scan a spatially resolved laser beam across the surface of a SiPM at cryogenic temperatures for the purposes of nEXO device uniformity testing.

Résumé

La découverte de masses non-nulles chez le neutrino nous force à confronter leur origine et leur nature. Les théories prédominantes aujourd'hui voudraient que le neutrino s'agisse d'une particule de Dirac, comme toutes les autres dans le modèle standard, ou alors de Majorana, une explication plus naturelle de la petitesse des masses en question. Cette seconde solution ferait du neutrino sa propre antiparticule et, par là même, ouvrirait la porte à des procédés en violation de la conservation du nombre leptonique. L'une des réactions candidates les plus prometteuses pour investiguer la possible nature Majorana du neutrino est la double désintégration bêta sans neutrinos. C'est l'objectif principal de la collaboration nEXO que de l'observer. La chambre à dérive de nEXO contiendrait 5 tonnes de xénon liquide enrichi à 90% de ^{136}Xe , isotope capable d'effectuer des doubles désintégrations bêta. L'énergie et la position de chaque événement seraient calculées d'après des signaux d'ionization et de scintillation. Pour détecter la lumière ultraviolette de ces derniers, des photomultiplicateurs en silicium (SiPMs) ont été sélectionnés. Il s'agit de détecteurs à semi-conducteurs de $\sim 1 \text{ cm}^2$ sensibles aux photons individuels, qui ici seraient placés en périphérie de la chambre à dérive. nEXO prévoit tapisser une surface totale de 4.5 m^2 , ce qui exigerait des milliers de SiPMs. Pour les tester à température de déploiement dans des délais raisonnables pour nEXO, une approche bien huilée reposant sur des hauts débits doit être développée. Cette thèse présente les résultats de la mise en service d'un mécanisme automatisé de balayage laser en vue de tester des modules de SiPM à des températures cryogéniques à des fins de tests d'uniformité pour nEXO.

Acknowledgments

First and foremost, my thanks to my supervisor, Dr. Thomas Brunner, for managing the feat of cheerfully guiding me despite the (sometimes mandatory) distance and through several (sometimes happy) major medical events. My thanks also to David Gallacher, who saw me through MIDAS integration and spared me many headaches; to Lucas Darroch, who kindly repeated the basics of SiPMs to me more times than I can count; to Dr. Chris Chambers, who taught me where everything was and helped me with optics; and to Dr. Sarah Nowicki, who provided a salutary framework during the writing of this thesis. Furthermore, I would like to thank the rest of the Brunner lab group, who were my first point of contact with the welcoming and vibrant physics community I found here at McGill.

Finally, on a personal level, I am much indebted to Andrea Salas, who pulled me through the ending; and, eternally, to my parents. Thank you.

Contribution of Authors

The electronics on both implementations of the Optical Rail System, described in Chapter 4, are based on work previously completed by Megan Cvitan and Tianyang Tim Yu, modified by the author. Furthermore, the Environmental Test Stand mentioned in Chapter 4 was designed and assembled as part of the MSc thesis of Lucas Darroch. MIDAS and MERCI, whose online analysis forms the basis of Chapter 5, were adapted for this project by David Gallacher. All sections of this thesis were written by the author, with the cited tables and figures adapted from references. All data was taken by the author.

Chloe Gingras

Montreal, July 2023

Contents

1	Physics Motivation	1
1.1	Neutrinos and the Standard Model	1
1.2	The Search for Majorana Neutrinos and $0\nu\beta\beta$	6
2	$0\nu\beta\beta$ Searches with EXO-200 and nEXO	11
2.1	The EXO-200 Experiment	11
2.2	The nEXO Experiment	13
3	Silicon Photomultipliers	19
3.1	Structure, Operation, and Response	19
3.2	Properties and Behaviours	22
3.3	Performance Requirements	23
3.4	SiPM Prototypes for nEXO	23
4	The Optical Rail System	28
4.1	Overview	28
4.2	Characterization of the Optical Rail System	32
4.2.1	Linear Stage: Motion Control and Calibration	33
4.2.2	Optics: Beam Spot Size	35
5	Results from Commissioning	39
5.1	Building a Raster Scan	40
5.2	SPAD-wise Scans	42
6	Conclusion and Outlook	49

List of Figures

1-1	Neutrino mass orderings	3
1-2	Fermion mass scales shown by generation	4
1-3	Simplified scheme of nuclear decays for nuclei with mass number $A = 136$. .	6
1-4	Feynman diagrams of regular and neutrinoless double beta decays	7
1-5	The $m_{\beta\beta}$ - m_{light} parameter space for both orderings	9
1-6	Electron kinetic energy spectrum for $2\nu\beta\beta$ and $0\nu\beta\beta$	10
2-1	The EXO-200 system	12
2-2	Preliminary design of the nEXO detector system	14
2-3	Time projection chamber for the nEXO experiment	15
2-4	nEXO's projected median sensitivity to $0\nu\beta\beta$ and its 3σ discovery potential	17
2-5	Effective Majorana neutrino mass sensitivity versus m_{light}	17
3-1	Single photon avalanche diode structure operated in fully depleted mode . .	19
3-2	Simplified equivalent circuit of a SiPM	20
3-3	Typical integrated pulse height spectrum of a low-count SiPM signal	21
3-4	Estimated energy resolution as a function of V_{OV} achievable by nEXO for FBK and Hamamatsu SiPMs	24
3-5	Several models of 4 th generation (VUV4) Hamamatsu SiPMs	25
3-6	PDE as a function of the wavelength for Hamamatsu VUV4 SiPMs	26
3-7	PDE at 175 nm as a function of V_{OV} for Hamamatsu VUV4 SiPMs	26
4-1	Schematic of the ORS setup	29
4-2	Basic schematic of a charge-sensitive preamplifier	29
4-3	Photos of the optics and motors in the Test-ORS	30
4-4	Photos of the optics and linear stage in the ETS-ORS.	31
4-5	Conceptual flow chart of the interactions and commands forming a scan cycle	32
4-6	Displacement consistency of the Test-ORS x-axis	33
4-7	Calibration results for the ETS-ORS and Test-ORS	34

4-8	Beam spot and elliptical fit to determine diameter	37
5-1	Typical pulses: signal intensity as a function of time for the laser trigger and SiPM signal, as displayed by MERCI’s online frontend during live analysis	39
5-2	Raster scan pattern	40
5-3	Signal amplitude distribution for all pulses recorded at a single stop point	41
5-4	Raster scan of a Hamamatsu VUV4 SiPM with a granularity of 100 μ m, showing fluctuations in signal amplitude, f_i	42
5-5	Error function fit of the signal at a SiPM edge	44
5-6	Signal amplitude distribution for a single SPAD	45
5-7	Scan of a single row of SPADs on a Hamamatsu VUV4 SiPM	45
5-8	Mean pulse amplitude versus time for all scan rows, consecutively	47
5-9	Relative PDE of a row of SPADs	48

List of Tables

1-1	Recent limits on $m_{\beta\beta}$ from different experiments	8
3-2	Some specifications for nEXO light detection and corresponding SiPM requirements in order to achieve a total energy resolution of $\lesssim 1\%$	23
3-3	Structural, electrical and optical properties of the Hamamatsu VUV4 S13371-6050CQ series	27
4-4	Conversion factors from motor step size to measured displacement, extracted from the calibration	36
4-5	Differing values in the optics subsystems of the Test-ORS and ETS-ORS	38
5-6	Parameters of the SPAD-wise scan	43
5-7	Standard deviation of signal amplitude fluctuations for the coarse scan, and for the SPAD-wise scan with and without hotspots	46

List of Abbreviations

CAF	Correlated avalanche fluctuation
CL	Confidence level
CSP	Charge-sensitive preamplifier
DAQ	Data acquisition system
ETS	Environmental test stand
FBK	Fondazione Bruno Kessler
FWHM	Full width at half maximum
HFE	Heat transfer fluid used in EXO-200 and planned for nEXO
LAAPD	Large-area avalanche photodiode
LXe	Liquid xenon
MERCI	Modular online multi-threaded C++ based waveform toolkit
MIDAS	Maximum Integrated Data Acquisition Structure
ORS	Optical rail system
PDE	Photon detection efficiency
PMNS	Pontecorvo-Maki-Nakagawa-Sakata
PMT	Photomultiplier tube
SiPM	Silicon photomultiplier
SM	Standard Model of Particle Physics
SPAD	Single photon avalanche diode
TPC	Time Projection Chamber
VUV	Vacuum ultraviolet
VUV4	Hamamatsu model 4 th generation silicon photomultipliers

1 Physics Motivation

Neutrinos are the most abundant known particle next to photons. The rarity of their interactions with the rest of the Standard Model (SM) particles is both obstacle to, and promise of, observing new physics: neutrinos do not interact through the strong nuclear force or through electromagnetic forces; they feel gravity but their mass is orders of magnitude smaller than any other SM particle; they only couple to the W and Z bosons, and thus with current capabilities they can only be detected indirectly through weak interactions.

1.1 Neutrinos and the Standard Model

A Short History

When he first introduced the neutrino in 1930, Pauli famously expressed misgivings about postulating the existence of an undetectable particle. These were put to rest in 1956, when the neutrino was experimentally detected by Cowan and Reines [1]; the neutrino was at this time included into the SM as massless. In 1995, Reines would be awarded the Nobel Prize “for the detection of the neutrino” and “for pioneering experimental contributions to lepton physics” [2] (Cowan, having died, was no longer eligible). However, these early massless models were soon challenged by experimental evidence, and incorporation of neutrino mass into the SM is still ongoing.

In the 1960s, the Homestake experiment revealed a major discrepancy between the expected and measured solar neutrino flux [3]. The measured flux in the Homestake experiment fell two-thirds short of expected values; subsequent experiments confirmed the deficit. This was all the more shocking as the involved stellar nuclear processes were well established at the time, yielding no leeway on theoretical predictions [4, 5]. Nonetheless, Raymond Davis Jr., who headed the Homestake experiment, would be jointly awarded one half of a divided Nobel prize in 2002 “for pioneering contributions to astrophysics, in particular for the detection of cosmic neutrinos” [5, 6].

The solar neutrino problem, as it was dubbed, was only solved at the turn of the millennium upon confirmation of neutrino oscillations [7, 8] — eventually resulting in another Nobel prize, awarded jointly to Takaaki Kajita and Arthur B. McDonald in 2015, “for the discovery of neutrino oscillations, which shows that neutrinos have mass” [9]. By that time, three distinct neutrino states had been detected through charged-current interactions with leptons e , μ , and τ . The intrinsic property of flavour is conserved in these interactions and thus the corresponding respective charged-current-interaction eigenstates (or flavour eigenstates) of neutrinos are designated ν_e , ν_μ , and ν_τ . Neutrino oscillations allow for transitions between them by having neutrinos *interact* as flavour eigenstates, but *propagate* through spacetime as distinct but overlapping *mass* eigenstates as described by:

$$\begin{bmatrix} \nu_e \\ \nu_\mu \\ \nu_\tau \end{bmatrix} = \begin{bmatrix} U_{e1} & U_{e2} & U_{e3} \\ U_{\mu1} & U_{\mu2} & U_{\mu3} \\ U_{\tau1} & U_{\tau2} & U_{\tau3} \end{bmatrix} \begin{bmatrix} \nu_1 \\ \nu_2 \\ \nu_3 \end{bmatrix} \quad (1)$$

where ν_i ($i \in \{1, 2, 3\}$) refer to mass eigenstates and $U_{\alpha i}$, α being a flavour eigenstate, are the entries of the Pontecorvo–Maki–Nakagawa–Sakata (PMNS) matrix [10]. Thus, mass eigenstates are the eigenstates of the free-particle Hamiltonian and can be expressed as linear combinations of flavour eigenstates just as, conversely, flavour eigenstates can be expressed as linear combinations of mass eigenstates.

The probability for transitions between flavour eigenstates, as a function of time, depends on the coefficients of the PMNS matrix and on mass splittings $\Delta m_{ij}^2 = m_i^2 - m_j^2$ ($i \neq j$) [11]. With three mass eigenstates, only two mass splittings are independent. There follow two possible mass orderings: normal and inverted, illustrated, along with the approximate flavour contents of each mass eigenstate, in Fig. 1-1. By convention, m_1 and m_2 are the most closely spaced, and therefore the lowest mass state is m_1 in the normal ordering scenario and m_3 in the inverted ordering scenario. Oscillation experiments currently favour the normal ordering [12], but settling the question will require increased sensitivity.

Mass splitting values can be determined from the study of oscillations in neutrinos from specific sources. Solar neutrino experiments like SNO and Super-Kamiokande yield $(m^2)_{\text{sol}} \simeq 7.6 \times 10^{-5} \text{ eV}^2$; atmospheric neutrino experiments like ANTARES and IceCube yield $(m^2)_{\text{atm}} \simeq 2.5 \times 10^{-3} \text{ eV}^2$ [13]. Fig. 1-1 identifies these for both orderings. Besides solar neutrinos and atmospheric neutrinos, the two other major sources used in experiments are neutrinos from reactors and accelerators [12].

Neutrino flavour oscillation experiments only measure mass squared differences, Δm_{ij}^2 , and are insensitive to the absolute mass scale of the neutrino; in particular, they allow mass scales to reach values higher than the determined $\sqrt{\Delta m_{ij}^2}$ [12]. The mass scale must therefore be probed with other types of experiments. Cosmology constrains the sum of neutrino masses, $\sum m_{\nu_\alpha}$ [14, 15], but the only model-independent way of determining neutrino masses is to exploit constraints on the kinematics of weak decays involving a neutrino or an antineutrino [12]. The KATRIN experiment performs these direct kinematic searches in tritium decay. Results published in 2022 set a limit of $m_{\nu_e} < 0.8 \text{ eV}/c^2$ at a 90% confidence level (CL) [16].

Future Prospects: Beyond the Standard Model

While the introduction of nonzero neutrino mass addresses neutrino oscillation and solves the solar neutrino problem, it imposes the further necessity of incorporating these nonzero masses into the SM with appropriate extensions. Massive neutrinos can be minimally accommodated through the Dirac mechanism, like all other fermions — that is, through a Yukawa coupling

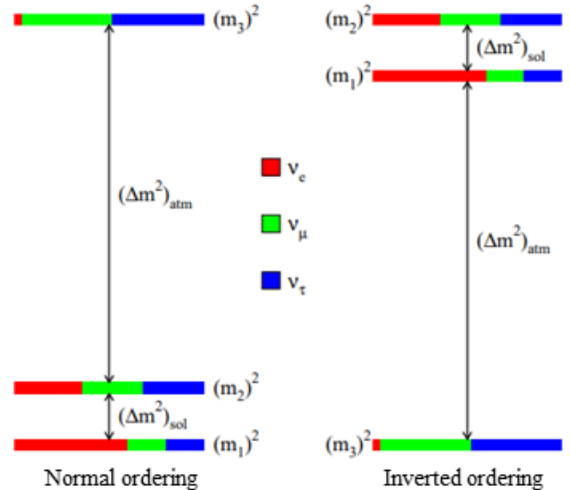


Figure 1-1: Neutrino mass orderings which broadly fit current data. Colours indicate the fraction $|U_{\alpha i}|^2$ of each flavour α in each mass eigenstate i . Figure adapted from [11].

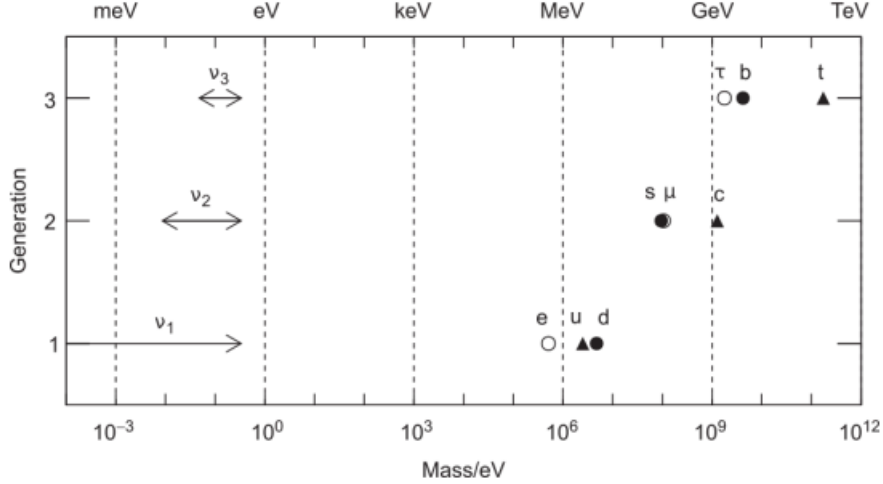


Figure 1-2: Fermion mass scales shown by generation, assuming a normal ordering for neutrinos. Having been experimentally constrained to the sub-eV scale, neutrino masses are $\gtrsim 6$ orders of magnitude below those of the other fermions in their respective generations. Under a Dirac mass framework, this requires an outstandingly small coupling to the Higgs. Adapted from [17].

with the Higgs field. The associated SM Lagrangian Dirac mass term, \mathcal{L}^D , is [17]

$$\mathcal{L}^D = -m_D (\bar{\nu}_R \nu_L + \bar{\nu}_L \nu_R), \quad (2)$$

where m_D is a Dirac mass and ν_L and $\bar{\nu}_R$ are left- and right-handed chiral projections corresponding to neutrino and antineutrino fields.

However, the Dirac explanation is theoretically unappealing. First, it fails to address the sub-eV scale of neutrino mass, which makes it a distant outlier compared to other SM fermion masses, as shown in Fig. 1-2, and would therefore require an outstandingly small coupling to the Higgs. Second, it introduces non-interacting, heavy right-handed neutrinos, ν_R , which have yet to be observed.

By contrast, the so-called Majorana mass mechanism provides more satisfactory solutions. For a single generation, its SM Lagrangian, \mathcal{L}^M , is [17]

$$\mathcal{L}^M = -\frac{1}{2} m_M ((\bar{\nu}_R)^c \nu_R + (\bar{\nu}_R) \nu_R^c), \quad (3)$$

where m_M is the Majorana mass and $(\nu_R)^c$ is the left-handed antineutrino field. This mechanism coexists with the Dirac mechanism, and both can simultaneously be included in the SM Lagrangian under a general set of neutrino mass terms. Combining Eqns. 2 and 3 and rewriting them in matrix form, we get

$$\mathcal{L} = -\frac{1}{2} \begin{bmatrix} \bar{\nu}_L & \bar{\nu}_R^c \end{bmatrix} = \begin{bmatrix} 0 & m_D \\ m_D & m_M \end{bmatrix} \begin{bmatrix} \nu_L^c \\ \nu_R \end{bmatrix} + \text{h.c.}, \quad (4)$$

where h.c. is the Hermitian conjugate [17]. The matrix's eigenvalues give the physical masses: in the $m_M \gg m_D$ limit, they reduce to approximately $m_{\text{heavy}} = m_M$ and $m_{\text{light}} = m_D^2/m_M$, respectively the right-handed and left-handed neutrinos.

Models which dramatically drive down m_{light} by channeling the extra mass into m_{heavy} in this way fall under the umbrella term of “seesaw mechanism.” A variety of Majorana-type extensions to the SM have been formulated, but the seesaw mechanism currently enjoys widespread favour for its concinnity with the SM. Beyond suppressing the lighter mass, it allows the neutrino to couple to the Higgs with strengths comparable to other fermions and it further explains the absence of observations for heavy right-handed neutrinos [18].

Regardless of model, a Majorana component to the neutrino mass would lead to entirely new physics. For one, it would provide a new mechanism for mass generation involving wholly different mass scales [17]. In addition, as Eq. 3 shows, Majorana mass creates a path for direct coupling between particle and antiparticle states, allowing for neutrino to antineutrino transitions — effectively making the neutrino its own antiparticle. This would constitute a new class of fundamental particle, as the nonzero charge of all other fundamental fermions forces particles and antiparticles to be distinct. Finally, Majorana mass opens the door to leptogenesis, a mechanism for matter to be created without equal amounts of antimatter, and thus may explain the baryon asymmetry. These theoretical implications drive current searches for Majorana neutrinos, as described in the following section.

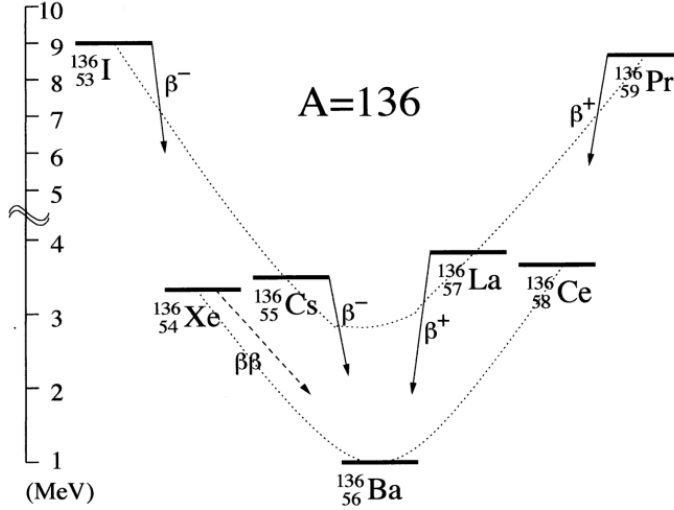


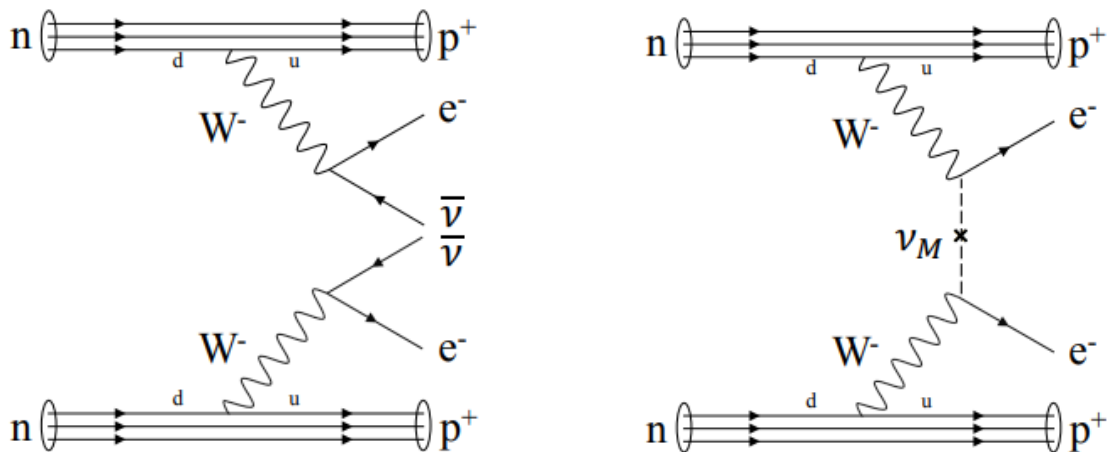
Figure 1-3: Simplified scheme of nuclear decays for nuclei with mass number $A = 136$. Among even nuclei, odd-odd and even-even nuclei have distinct stability parabolas (dotted lines), attributed to the pairing energies of nucleons. For ^{136}Xe , β decay to ^{136}Cs is energetically disfavoured. Instead, it decays to ^{136}Ba through $\beta\beta$ decay. From [20].

1.2 The Search for Majorana Neutrinos and $0\nu\beta\beta$

If realized in nature, Majorana mass would result in a new decay channel, neutrinoless double beta decay ($0\nu\beta\beta$), in isotopes that already undergo double beta decay ($2\nu\beta\beta$). First proposed by Maria Goeppert Mayer [19], $2\nu\beta\beta$ is a rare but established SM process whereby even-even nuclei decay to a lower energy state by undergoing two beta decays simultaneously when single beta decay is suppressed. Fig. 1-3 illustrates why double beta decays are favoured over single decays in ^{136}Xe .

$0\nu\beta\beta$ is a hypothetical analogous process without neutrino emission, which rests on the neutrino-antineutrino transitions made possible by Majorana mass. The Feynman diagrams in Fig. 1-4 highlight this key difference. If $0\nu\beta\beta$ is observed, then, per the Schechter–Valle theorem [23], the neutrino mass has a Majorana component, and lepton number is not conserved, contrary to SM predictions [24]. Lepton number conservation is thought to be a law in the SM, but theory does not require it; it may be violated by the net increase in lepton number which neutrino-antineutrino transitions allow.

The current lower bound on the $0\nu\beta\beta$ half-life is $T_{1/2}^{0\nu} \geq 10^{26}$ years [12]. Depending on



(a) $2\nu\beta\beta$, where two antineutrinos $\bar{\nu}$ are emitted. This process is permitted in the SM and had been observed in 14 isotopes as of 2019 [21].

(b) $0\nu\beta\beta$, where interactions among Majorana neutrinos, ν_M , would result in no outgoing neutrinos. The decay does create two outgoing leptons.

Figure 1-4: Feynman diagrams of (a) regular and (b) neutrinoless double beta decays. Reproduced from [22].

the model, measurements of $T_{1/2}^{0\nu}$ may limit or determine the effective Majorana neutrino mass, defined as [25]:

$$m_{\beta\beta} \equiv \sum_i (U_{ei})^2 m_i. \quad (5)$$

In particular, in the light-neutrino exchange model (the most widely accepted [25]), the half-life of $0\nu\beta\beta$ is given by:

$$T_{1/2}^{0\nu} = (\mathcal{G}|\mathcal{M}|^2 m_{\beta\beta}^2)^{-1}, \quad (6)$$

where \mathcal{G} is the phase-space factor and \mathcal{M} contains the nuclear matrix elements, whose modeling and computation are finely tuned to the data. The effective Majorana neutrino mass thus explicitly relates elements of theory to observables.

In addition, $m_{\beta\beta}$ enables (imperfect) comparisons of the physics reach of different experiments — in particular, those searching for $0\nu\beta\beta$ in different isotopes. Several experiments have searched for $0\nu\beta\beta$ among candidate isotopes, most notably ^{76}Ge , ^{136}Xe , ^{100}Mo , and isotopes of Te [26].

Most of these experiments use a common approach of surrounding with detectors a large

mass of the candidate isotope: the greater the active mass and the longer the experiment runtime, the greater the discovery potential (or, short of discovery, the lower the exclusion limits). So far, experiments have constrained the parameter space by lowering the upper bounds on neutrino mass. Table 1-1 compares recent exclusion limits obtained by $0\nu\beta\beta$ experiments searching in different isotopes. Fig. 1-5 illustrates the constraining of parameter space by oscillation experiments for both mass orderings. Next-generation experiments aim for the sensitivity to cover the inverted ordering region and reach into the normal ordering region [15].

Experiment	Isotope	Sensitivity ($\times 10^{25}$ yr)	$m_{\beta\beta}$ (eV)	
Aurora	^{116}Cd	(-)	$< 1.0 - 1.7$	[27]
CUORE	^{130}Te	2.8	$< 0.09 - 0.31$	[28]
CUPID-0	^{82}Se	0.5	$< 0.31 - 0.64$	[29]
CUPID-Mo	^{100}Mo	(-)	$< 0.31 - 0.54$	[30]
ELEGANT VI	^{48}Ca	1.8×10^{-3}	$< 3.5 - 22$	[31]
EXO-200	^{136}Xe	5.0	$< 0.09 - 0.29$	[32]
GERDA	^{76}Ge	18	$< 0.08 - 0.18$	[33]
KamLAND-Zen	^{136}Xe	23	$< 0.036 - 0.156$	[34]
Majorana Demonstrator	^{76}Ge	4.8	$< 0.113 - 0.269$	[35]
NEMO-3	^{150}Nd	(-)	$< 1.6 - 5.3$	[36]
NEMO-3	^{96}Zr	(-)	$< 7.2 - 19.5$	[37]

Table 1-1: Recent limits on $m_{\beta\beta}$ from different experiments, each with their own isotopes and detector technologies [26].

The Kinetic Energy Spectrum: A Search Method

In experiments which search for $0\nu\beta\beta$, event energy is crucial: whether or not antineutrinos are produced, under current capabilities, they go undetected, and therefore only electron kinetic energy K_{e^-} distinguishes $0\nu\beta\beta$ from $2\nu\beta\beta$. In both, nuclear recoil is negligible and the leptons carry virtually all available energy [20]. Fig. 1-4a shows that in $2\nu\beta\beta$, the energy corresponding to the Q-value of the decay is shared between the antineutrinos and the electrons; this results in a continuous spectrum for possible K_{e^-} values. By contrast, per Fig. 1-4b, in $0\nu\beta\beta$ the entirety of the available energy goes into K_{e^-} , resulting in a sharp

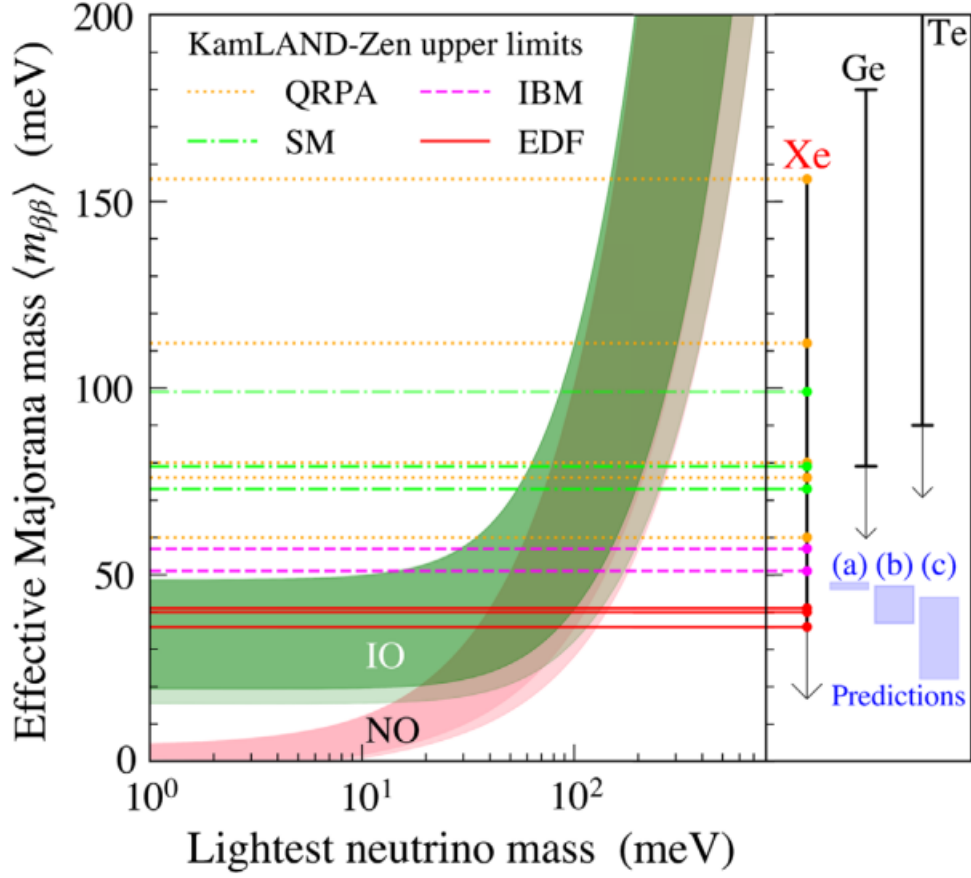


Figure 1-5: The $m_{\beta\beta}$ - m_{light} parameter space for both orderings (where m_{light} is unconstrained). Dark shading indicates predictions from best-fit values on oscillation parameters, and light shading indicates 3σ uncertainties. Below the horizontal lines are the regions allowed at 90% CL for various estimates of the nuclear matrix elements, with ^{136}Xe from the KamLAND-Zen experiment. The panel on the right compares the corresponding limit on $m_{\beta\beta}$ values to those of Ge and Te isotopes, as well as several model predictions; see [34] for details. From [34].

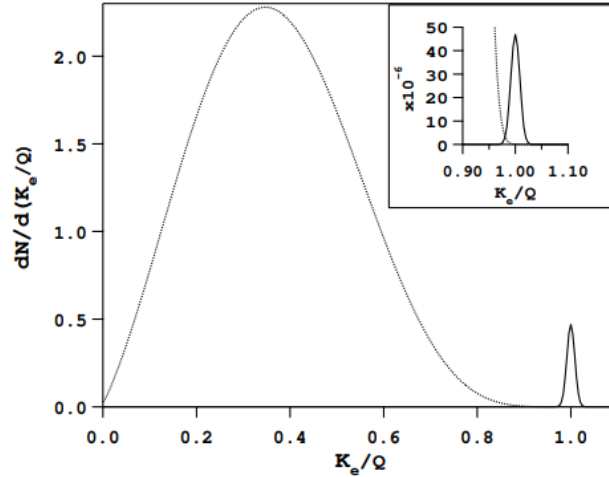


Figure 1-6: Electron kinetic energy spectrum for $2\nu\beta\beta$ (dotted curve) and $0\nu\beta\beta$ (solid curve). The abscissa are normalized to the maximum available energy, i.e., the Q-value. $0\nu\beta\beta$ signal is enlarged for visibility, given the decay's large half-life. 10^2 2ν decays are assumed for each 0ν decay; in the inlay, 10^6 2ν per 0ν . From [20].

peak at the Q-value. The contrast between this sharp peak and the wide $2\nu\beta\beta$ distribution is illustrated in Fig. 1-6, which shows the expected summed K_{e^-} spectra for both decays. Limits on the experimental energy resolution result in a peak at the Q-value.

If measuring the kinetic energy of the electrons provides a search method for $0\nu\beta\beta$, this method relies heavily on the good energy resolution of the detector. The following chapter describes EXO-200 and nEXO, respectively past and planned experiments relying on measurement of the kinetic energy spectrum.

2 $0\nu\beta\beta$ Searches with EXO-200 and nEXO

Among the experimental approaches to search for $0\nu\beta\beta$, both the EXO-200 and the nEXO experiments employ ^{136}Xe in a liquid-xenon time-projection chamber (TPC).

As a medium, liquid xenon presents several advantages. Noble elements are inert and do not form new chemical species, and among the noble liquids, xenon's atomic number ($Z = 54$, the highest of the stable rare gases) and density ($\sim 3 \text{ g/cm}^3$) impart it with the highest stopping power for penetrating radiation [38]. It also has the highest ionization and scintillation yield of all liquid noble gases, and thus produces substantial signal [38, 39]. The $0\nu\beta\beta$ decay of ^{136}Xe is:

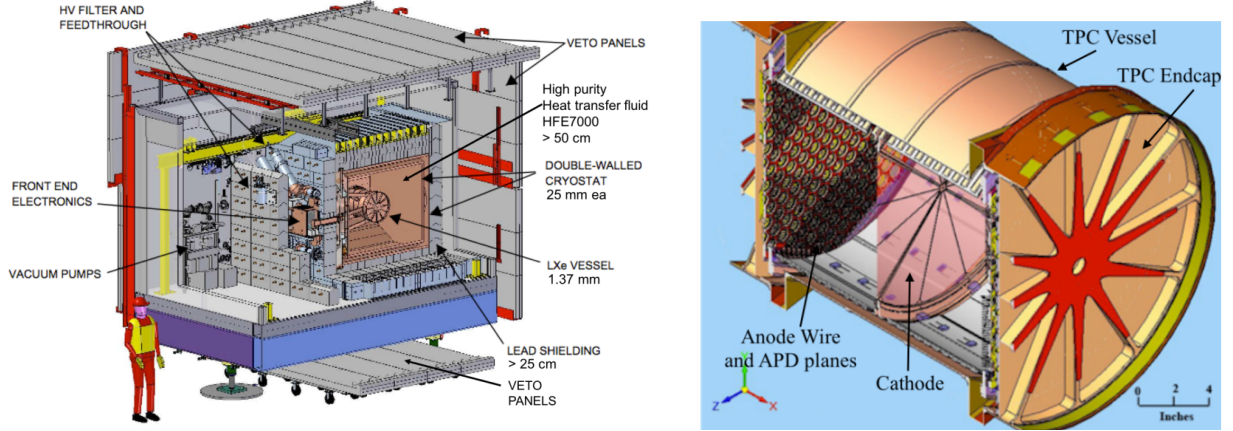


The Q -value of this decay, $Q = 2458.07 \pm 0.31 \text{ keV}$ [12], is located in a region with few naturally occurring radioactive backgrounds, which makes ^{136}Xe an attractive candidate [40]. Enrichment of natural xenon, with its relatively large abundance of ^{136}Xe ($\sim 8.8\%$), can be performed easily by centrifuges for high gas volumes [41].

2.1 The EXO-200 Experiment

The now-retired EXO-200 experiment had the double distinction of being the first experiment to observe $2\nu\beta\beta$ in ^{136}Xe , establishing its half-life as 2.165×10^{21} years [39], and of placing an (at the time) highly competitive upper limit on the half-life of $0\nu\beta\beta$ in ^{136}Xe . The experiment ran for a total livetime of 1181.3 days from 2011 to 2018, successively publishing higher limits on $0\nu\beta\beta$ half-life as sensitivity improved, for a final value of 3.5×10^{25} years at the 90% confidence level [32].

Located underground inside a mine drift at the Waste Isolation Pilot Plant in New Mexico, EXO-200 was shielded by an overburden of 1624 meters of water equivalent (m.w.e) and housed in a class 1000 clean room [42]. An array of plastic scintillator pannels provided an active muon veto, and within the clean room, low-radioactivity lead blocks acted as



(a) The EXO-200 setup: the LXe vessel, a TPC, is immersed in a HFE-7000 bath, itself in a lead-shielded cryostat. Front-end electronics sit outside the lead shielding. The detector assembly is located in a clean room surrounded by muon veto panels.

(b) The EXO-200 TPC: a cathode splits the vessel into two mirrored TPCs with anodes at each end for charge detection. Arrays of LAAPDs sit behind the anodes for light detection.

Figure 2-1: The EXO-200 system: the underground installation and the TPC. From [22].

passive shielding to a vacuum insulated cryostat; the inner cryostat contained a bath of heat transfer fluid, HFE-7000, for thermal moderation and pressure regulation, with bonus added passive shielding, and, finally, the TPC. Fig. 2-1a shows a cutaway view of the EXO-200 underground experimental setup.

Fig. 2-1b shows a detailed schematic of the EXO-200 detector’s TPC: a time projection chamber (TPC) containing an active mass of ~ 110 kg of liquid xenon (LXe) enriched to 80.6% in ^{136}Xe [39]. Noble liquid time projection chambers are suitable for extremely low background operations, and they offer the advantages of scalability and response uniformity in monolithically sensitive volumes [25]. In EXO-200, both ends of the cylindrical TPC were anode wire planes held at virtual ground. Between them, a common cathode with 90% optical transparency, held at -8 kV [40], effectively split the volume evenly into twin TPCs. A field shaping cage ensured a uniform drift field between the cathode and the anodes. Both anodes were composed of an induction plane and a collection plane, each plane allowing position reconstruction along one dimension, and jointly allowing spatial reconstruction of the charge cloud on the anode plane. Behind the anode wire planes were arrays of large-

area avalanche photodiodes (LAAPDs) for light collection [43]; these were selected over conventional photomultiplier tubes (PMTs) for their compact size, low radioactivity, and high quantum efficiency at xenon scintillation wavelengths [43]. The time difference between charge ($\sim \mu\text{s}$ timescale) and scintillation ($\sim \text{ns}$ signal detection), combined with the known drift velocity, allows the reconstruction of the lateral position of the event within the TPC [44]. Furthermore, light and charge yields are anti-correlated [44], which reduces statistical fluctuations between both channels. EXO-200 was the first to demonstrate that this can be used to enhance the energy resolution of LXe detectors.

EXO-200 also produced pioneering results demonstrating the power of monolithic detectors to identify and reject backgrounds, and its impact on detector sensitivity. Notably, EXO-200 showed that the background rejection capabilities of LXe TPCs, which placed emphasis on identifying γ background events, improved using event topology; and EXO-200's background modeling, which combined rigorous radioassay programs with detector simulations, proved highly successful [45, 46]. EXO-200 also demonstrated the viability of rare event searches in LXe TPCs, afforded collaboration members experience in building them, and laid the groundwork for the nEXO experiment, its proposed successor.

2.2 The nEXO Experiment

nEXO aims to observe $0\nu\beta\beta$ decay in ^{136}Xe , like EXO-200. By improving upon technologies validated by EXO-200, it plans to achieve beyond 10^{28} year half-life sensitivity at 90% CL after a decade of data collection, corresponding to a $m_{\beta\beta}$ mass range of $\sim 6 - 18$ meV (depending on the computation of nuclear matrix elements) [47]. To reach this sensitivity, the experiment aims for $\leq 1\%$ energy resolution at the Q-value.

Overview

nEXO is anticipated to be located at the cryopit of SNOLAB, in Ontario. The cryopit is located in an active mine, 2 km underground, which provides ~ 6010 m.w.e of shielding from

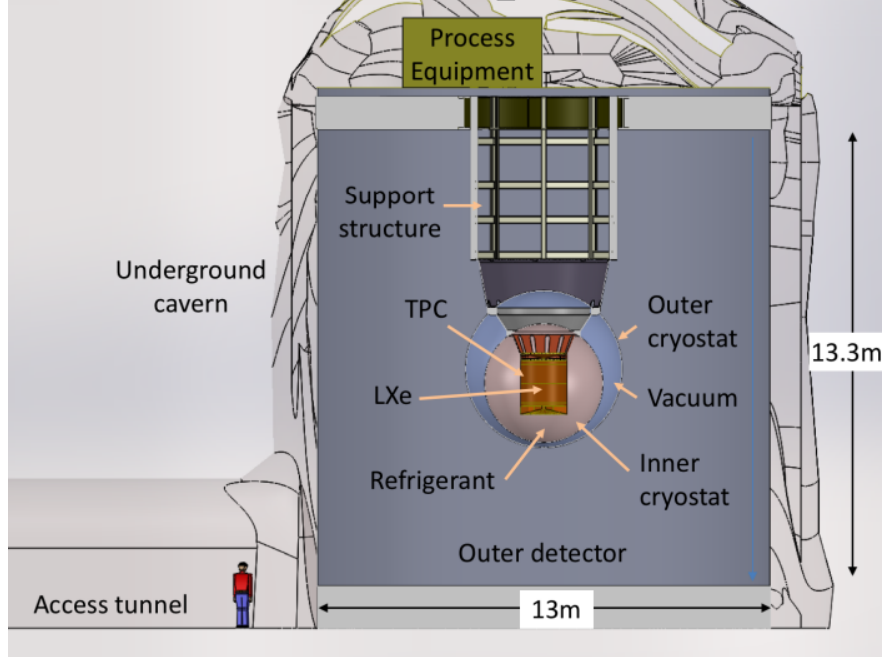


Figure 2-2: Preliminary design of the nEXO detector system. The 5-tonne TPC is shielded by two cryostats: one containing heat transfer fluid, which doubles as a γ shield, and the other, a vacuum. The outer detector provides further shielding and an active muon veto. The assembly is located in SNOLAB’s underground cryopit. From [22].

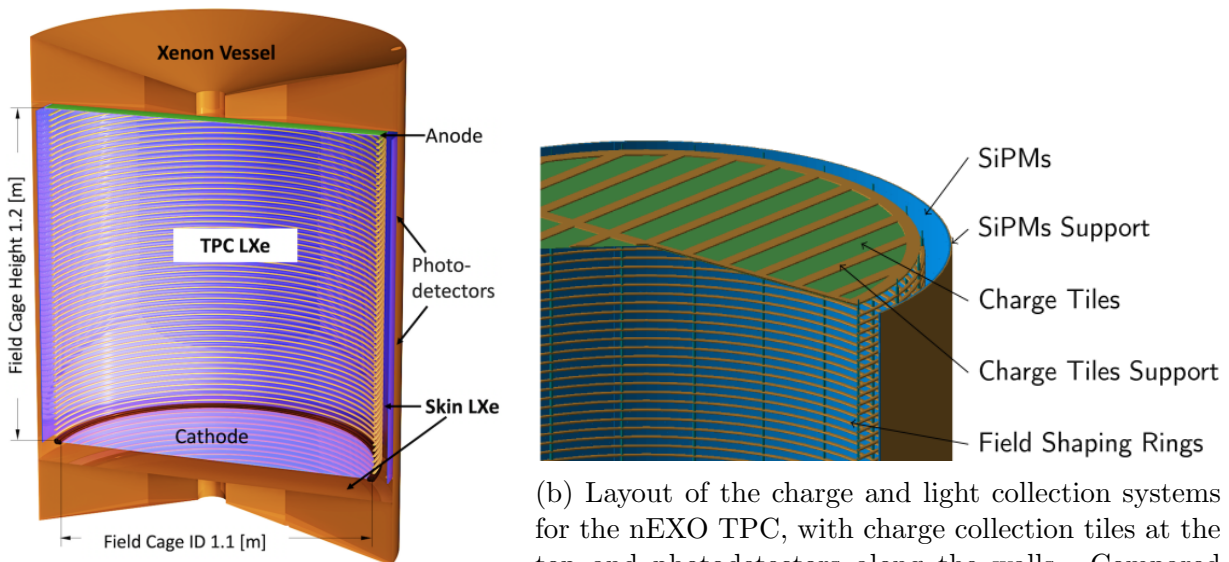
cosmogenic backgrounds [48]. However, the surrounding rock contains high levels of naturally occurring ^{238}Th and ^{238}U , whose radioactive decays generate backgrounds and require both passive shielding and monitoring. nEXO’s background model also includes solar neutrinos interacting in the detector, decay products of ^{222}Rn (present in steady-state in the LXe), and radionuclides created both by interactions with cosmic radiation and by (α, n) interactions from α -unstable isotopes such as ^{222}Rn [22].

Fig. 2-2 outlines the main components of the nEXO detector system. The outer detector, a tank of purified water instrumented with PMTs, shields the inner assembly from environmental radiation and tags muons by their Cherenkov radiation, providing an active muon veto. Inside, an outer cryostat upholds thermal insulation from the water tank by way of a vacuum; an inner cryostat filled with cryogenic fluid maintains thermal uniformity and provides further shielding.

At the heart of the assembly is the Xe-filled TPC, which relies on concepts and technology

first elaborated for EXO-200: a detector with charge and light collection capabilities. As in EXO-200, the anti-correlation between the two channels allows for optimization of the energy resolution: the $\leq 1\%$ design goal is based on an assumption of optimized anti-correlation. This calculation is laid out in Ref. [47].

Unlike EXO-200, however, the nEXO detector is monolithic. Furthermore, for increased sensitivity, the active mass is scaled up to 5 tonnes of LXe, 90% enriched to ^{136}Xe . The need for higher xenon purity derives from the higher volumes and longer electron drift lengths in the nEXO TPC, whose diameter is of 115 cm and whose drift length is 125 cm [22]. Fig. 2-3a shows a cross-section of the nEXO TPC.



(a) Cross-section of the entire nEXO TPC, with electrodes at the edges and photodetectors (i.e., SiPMs) on the walls. From [49].

(b) Layout of the charge and light collection systems for the nEXO TPC, with charge collection tiles at the top and photodetectors along the walls. Compared to EXO-200, this layout allows for larger coverage: EXO-200 had a total photocoverage area of 0.094 m^2 , whereas nEXO has $\sim 4.6 \text{ m}^2$ [43, 50]. Adapted from [22].

Figure 2-3: Time projection chamber for the nEXO experiment.

Light and Charge Collection

In the monolithic nEXO TPC, the cathode, located at the bottom, generates a static electric field to drift electrons to the anode, consisting of charge tiles, at the top, as shown in Fig. 2-3a [46, 51]. These charge tiles, which collect electrons, are made of dielectric material; a

simulation of the charge reconstruction performance of this anode design can be found in [52]. Because background-producing ^{222}Rn daughters drift to the electrodes, a TPC design which keeps the cathode at the edge of the LXe volume, rather than inside it as EXO-200 did, minimizes their impact [22]. The detector being monolithic has the added benefit of reducing background contributions at $Q \pm 2\sigma$ compared to EXO-200, since greater volumes require proportionally less shielding volume.

To detect the vacuum ultra-violet (VUV) 174.8 nm [47] scintillation light of liquid xenon, the nEXO collaboration has selected silicon photomultipliers (SiPMs). This technology was still in development during the EXO-200 design phase [53], but has since matured into a favourite contender for noble-liquid photodetection in general. In nEXO, individual SiPMs with an area of $\sim 1 \text{ cm}^2$ are arranged in groups, themselves read out as individual channels; channels are arranged in $\sim 10 \times 10 \text{ cm}^2$ tile modules; and tiles are mounted on vertical staves on the TPC barrel surface behind the field-shaping rings, as in Fig. 2-3b, for a total photocoverage area of $\sim 4.6 \text{ m}^2$ [50]. One front-end ASIC per SiPM tile transports signals out of the detector in digitized form using low radioactivity cables. Cryogenic, radiopure ASICs are currently under development, and their infrastructure is a focus of nEXO R&D efforts [50].

nEXO's Projected Sensitivity

The advances in design and data analysis from EXO-200 contribute to nEXO's improved sensitivity. Its projected sensitivity is shown as a function of experiment livetime in Fig. 2-4. After a nominal 10-year exposure, the 3σ discovery potential is $T_{1/2}^{0\nu} = 0.74 \times 10^{28} \text{ yr}$ and the absence of an observed signal will point to an exclusion of $T_{1/2}^{0\nu} > 1.35 \times 10^{28} \text{ yr}$ at 90% CL [47].

Assuming the light-neutrino exchange model mentioned in Chapter 1, half-life sensitivity translates to a range for $m_{\beta\beta}$ at 90% CL. Fig. 2-5 shows the resulting exclusion sensitivity regions of EXO-200 and nEXO as a function of m_{light} (m_{min} in the figure), for both mass

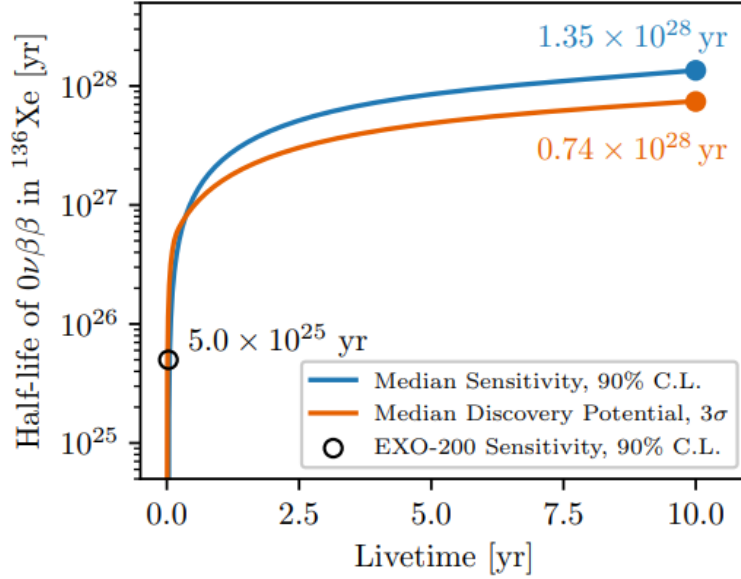


Figure 2-4: nEXO’s projected median sensitivity to $0\nu\beta\beta$ and its 3σ discovery potential. The collaboration aims for a 10-year livetime. From [47].

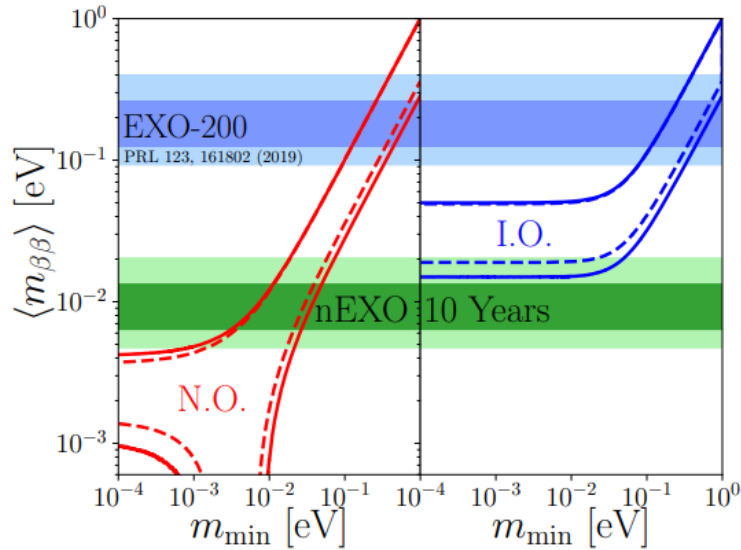


Figure 2-5: Effective Majorana neutrino mass sensitivity versus $m_{\min}(=m_{\text{light}})$ for both mass orderings, at 90% CL. The widths on the bands stem from the range of values of nuclear matrix elements used in calculations; the darker bands cover $\sim 68\%$ of values. This figure echoes Fig. 1-5, and highlights the reach of EXO-200 and nEXO, including where the latter exceeds the inverted ordering. From [47].

orderings.

These sensitivities, as well as nEXO's stated goal of $\leq 1\%$ energy resolution at the Q-value, require efficient collection of both light and charge signals. To detect the scintillation light of ^{136}Xe , the nEXO collaboration has chosen SiPMs. Their integration into the larger experiment design is described above. Chapter 3 delves into further detail, and lays out their advantages, their principles of operation and their key parameters, as well as the specifics of the VUV-sensitive SiPMs used in this project.

3 Silicon Photomultipliers

3.1 Structure, Operation, and Response

Silicon photomultipliers are arrays of p-n junction photodiodes used to detect signals as low as individual photons with good timing resolution. They operate at low voltage, consume little power, are insensitive to magnetic fields, and are suitable to cryogenic temperatures [53]. Besides these advantages, several features make them particularly suited to detecting VUV light for nEXO, and justify the collaboration’s choice. nEXO’s radioactivity requirements bar the use of the more conventional PMTs [22], and compared to LAAPDs, SiPMs have higher gain (~ 4 orders of magnitude) and lower noise. SiPMs are typically square, which allows dense packing and high photocoverage, and their low mass per unit area and semiconductor-based fabrication enable their application in environments requiring low radioactive background levels [53].

The photodiodes comprising SiPMs are called single photon avalanche diodes (SPADs). Fig. 3-1 illustrates how they convert light into electrical signals: photons are absorbed in the absorption region, which allows the creation of electron-hole pairs in the depletion region.

Carriers drift to the avalanche region, where a very high field leads to impact ionization and yields additional e-h pairs, resulting in a chain reaction [53]. Both holes and electrons multiply — by analogy with the Geiger counter, this is referred to as Geiger mode — making the avalanche bidirectional (as opposed to, for instance, avalanche photodiodes, where impact ionization leads to electron-only avalanches). Notably, proportionality is lost: in Geiger mode, SPAD response is not

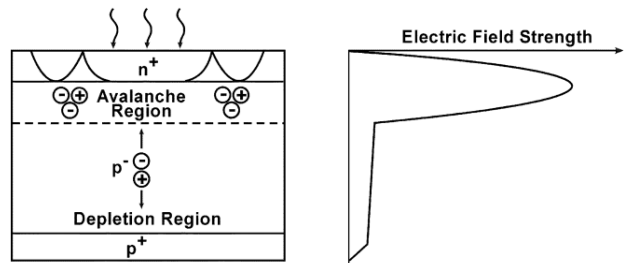


Figure 3-1: Single photon avalanche diode structure operated in fully depleted mode. On the left: photons create electron-hole pairs in the depletion region; carriers are accelerated to the avalanche region, where they multiply into an avalanche. On the right: the electric field strength in the p-n junction. Adapted from [54].

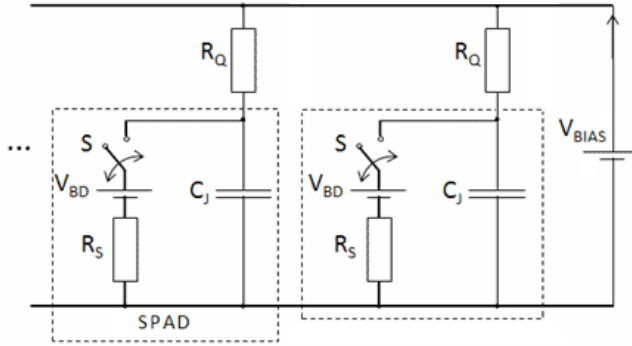


Figure 3-2: Simplified equivalent circuit of a SiPM with two SPADs, whose p-n junctions have a resistance R_S and a capacitance C_S . The switch S is open in the absence of light and closes when the avalanche begins. The quenching resistor R_Q stops the avalanche process. SiPMs are arrays of SPADs in parallel. Adapted from [55].

proportional to the initial number of pairs created. Nonetheless, this gain mechanism makes SPADs sensitive to single photons.

The operating range of SiPMs is defined by various voltages. Breakdown, V_{BD} , is the threshold for Geiger-mode avalanches. Applying an external bias, $V_{BIAS} > V_{BD}$, creates the depletion region. The main adjustable parameter which controls SiPM operation is the difference between the two, known as overvoltage: $V_{OV} = V_{BIAS} - V_{BD}$. At the runaway potential, $V_{RUNAWAY}$, SiPMs remain in a continuous state of avalanching [55].

SiPM response can be modeled by a simple electrical model. SPADs connect in parallel via resistors to serve as pixels to the larger arrays which constitute the SiPMs. Fig. 3-2 shows a simplified circuit schematic of this assembly. The formation of an e-h pair from a photon hit can be modeled as a switch, S , closing. This causes the p-n junction capacitance, C_J , to discharge through the resistance of the SPAD, R_S . As C_J discharges, impact ionization becomes less likely and the avalanche gradually stops (the bias voltage cannot perpetrate the avalanche further when the quenching resistor R_Q is chosen such that $R_S \ll R_Q$). Following the quenching, S opens, and the applied bias allows C_J to recharge. During the charge time, no additional photons can be detected. Recovery time, τ , is given by $\tau = R_S C_J$. Only once C_J is fully charged is the SPAD sensitive again for photon detection [55]. SiPM gain depends linearly on C_J and V_{OV} .

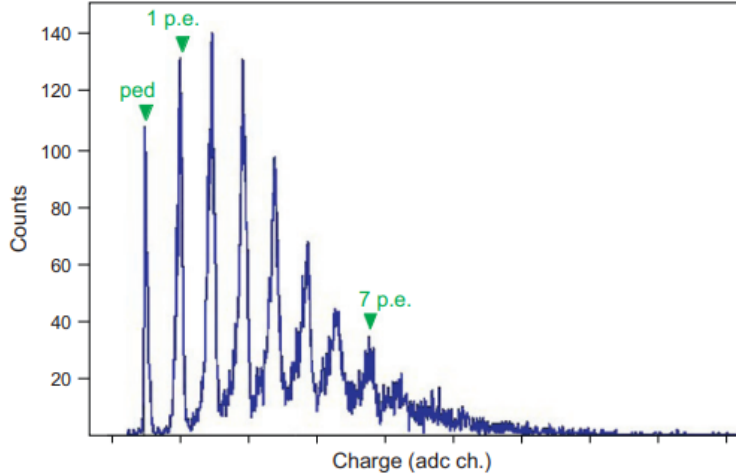


Figure 3-3: Typical integrated pulse height spectrum of a low-count SiPM signal. From the number of triggered pixels, the number of photoelectrons (p.e.’s) can be counted directly; the first peak, or “pedestal,” shows no pixels triggering. Adapted from [56].

Single photons are measured through two methods, both of which require sufficiently high gain: current measurement and pulse counting. In the former, typical SiPM gain ($\sim 1 \times 10^6$) yields low currents whose measurement limits the detectable photon rate. In opposition, pulse counting is not limited in that respect, but to be detected, the low voltage of single pulses requires amplification.

Collectively, pixels — SPADs — are read out by external electronics such that the resulting signal is an analog sum of all charges generated within each pixel. While these SiPM devices are pixelated, they do not function as image sensors.

At low counts, SiPM signals are usually integrated and displayed as histograms, like the one shown in Fig. 3-3, which highlights photon-counting capabilities. As the signal is proportional to the number of triggered pixels, each peak is (roughly) an integer multiple of the charge for the avalanche from one triggered pixel. It should be noted that the first peak denotes no pixels being triggered; the signal originates from electrical noise.

3.2 Properties and Behaviours

Besides gain and operational voltage, several properties define or impact SiPM performance, including photon detection efficiency (PDE), dark count, and correlated avalanches; corresponding requirements for the nEXO light detection system are listed in Table 3-2.

Photon detection efficiency constitutes the probability that a SiPM registers a photon hit. It is parametrized as:

$$\text{PDE} = \text{QE} \times \epsilon_{geo} \times P_{trigger}, \quad (8)$$

where QE is the quantum efficiency for the conversion of photons to electron-hole pairs in the p-n junction, ϵ_{geo} is the photosensitive area of the SiPM as a fraction of total SiPM area, and $P_{trigger}$ is the probability of an e-h pair triggering an avalanche. High gain, achieved through high overvoltage, increases the PDE while also increasing the dark count rate. Relative PDE, consisting of the PDE relative to a given reference, is also used to characterize SiPMs.

Dark counts result from free carriers in the depletion layer which were not triggered by an incoming photon, and they are indistinguishable from the signal of photon-induced avalanches. Generally, two main processes contribute to dark counts: thermally generated e-h pairs, which can be reduced by cooling, and field-assisted generation of free electrons, which has a smaller impact and can only be reduced by lowering the gain [53]. A SiPM's dark count rate is measured by securing the SiPM in a fully dark, light-tight environment, taking its charge spectrum, and calculating the time-averaged sum of ≥ 1 p.e. peaks.

Two processes are responsible for **correlated avalanches**: after-pulsing and cross-talk. The former occurs when charges become trapped in silicon impurities and are released with a delay; the latter occurs when secondary photons, emitted by sufficiently energetic carriers during an avalanche, travel to another SPAD and trigger it as well. This SPAD may be within the same SiPM or part of a neighbouring SiPM, corresponding respectively to internal and external cross-talk.¹ Either way, cross-talk is wavelength-dependent, as longer wavelengths

¹External cross-talk is particularly important in detector configurations where SiPMs are facing each other, such as in nEXO.

travel further in silicon. However, both effects generate secondary avalanches and for both, a probability of occurrence can be determined using statistical fluctuations. nEXO bases its requirements on a parameter called the Correlated Avalanche Fluctuation (CAF), defined as the ratio of the root mean square error to the average extra charge produced by correlated avalanches per pulse, within 1 μs of the primary pulse (see [47] for details).

3.3 Performance Requirements

The nEXO collaboration has set requirements for aforementioned performance parameters in order to achieve its stated aim of $\lesssim 1\%$ energy resolution at the Q-value; these key requirements are summarized in Table 3-2. The $\lesssim 1\%$ energy resolution places a lower bound on the total light collection efficiency, which itself requires the stated SiPM PDE; the lower bound on overvoltage is calculated from electronics noise requirements; the upper bounds on correlated avalanches are designed to minimize their contribution to resolution; and the bound on dark rate comes from the necessity for scintillation pulses to trigger at low energies (down to ~ 500 keV). See [22] for details.

Parameter	Value
Light collection efficiency	$\gtrsim 3\%$
SiPM PDE (175 nm, normal incidence)	$> 15\%$
Overvoltage	> 3 V
CAF rate	< 0.4
Dark noise rate	< 10 Hz/mm ²
Operational gain	$> 1.5 \times 10^6$

Table 3-2: Some specifications for nEXO light detection and corresponding SiPM requirements in order to achieve a total energy resolution of $\lesssim 1\%$ [22, 47].

3.4 SiPM Prototypes for nEXO

The nEXO collaboration has been driving R&D for VUV-sensitive SiPMs for a number of years. Photonics research companies Fondazione Bruno Kessler (FBK) and Hamamatsu

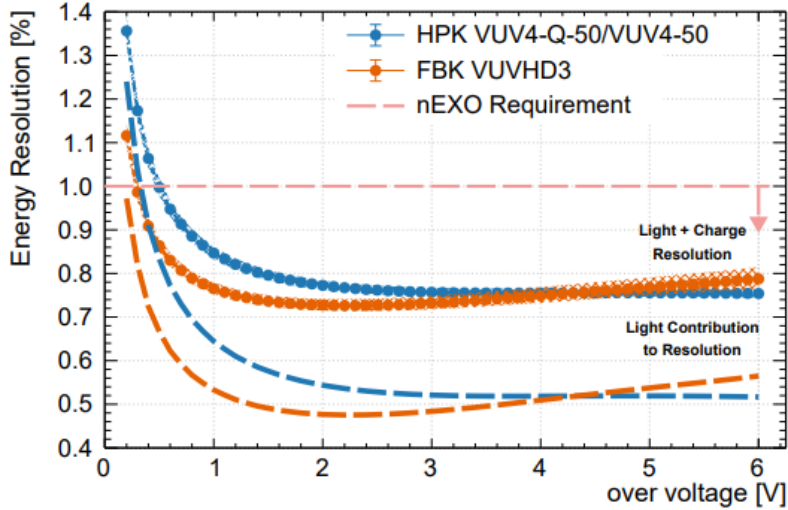


Figure 3-4: Estimated energy resolution achievable by nEXO as a function of V_{OV} for the latest generations of FBK and Hamamatsu SiPMs. Device models are the FBK VUVHD3, labelled as such, and Hamamatsu S13371-6050CQ and S13370-6050CN, labelled respectively HPK VUV4-Q-50 and VUV4-50. For the required $V_{OV} > 3$, all devices meet the energy resolution specifications. It should be noted that uncertainty bands on the combined light and charge energy resolution include some systematic effects and disregard others; see [47] for details. Furthermore, uncertainty bands have been omitted on the light-only dashed lines. From [47].

Photonics Inc. have produced several generations of SiPMs intended for nEXO, and continue to improve devices to meet or exceed nEXO standards.

The collaboration has performed studies on successive generations of devices to verify their adherence to the specifications laid out in Table 3-2 independently of manufacturer claims. In 2019, nEXO testing concluded that FBK SiPMs met those specifications, while Hamamatsu devices only just failed to meet PDE requirements [57, 58]. However, more recent testing shows that Hamamatsu 4th generation devices, referred to as VUV4s, meet all nEXO requirements [47].

Fig. 3-4 from nEXO’s 2022 study distils these latest results into estimations of the energy resolution achievable through devices from both companies. For $V_{OV} > 3$, the FBK model VUVHD3 and the Hamamatsu 4th generation (VUV4) models are all projected to meet the 1% energy resolution requirement, and indeed to exceed it. The FBK device performs better at low overvoltage due to its higher PDE, whereas in Hamamatsu VUV4 devices,

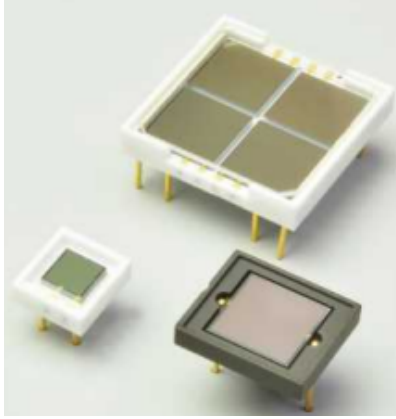


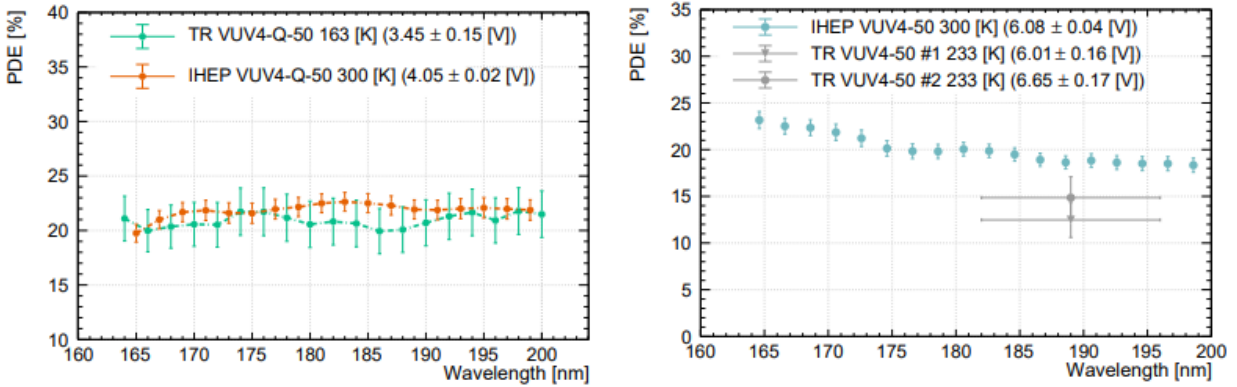
Figure 3-5: Several models of 4th generation (VUV4) Hamamatsu SiPMs. The uppermost SiPM is a S13371-6050CQ series, used in this project and designed to detect scintillation light from LXe. From [61].

correlated avalanches produce lower average extra charge per pulse, and thus they exhibit less degradation of energy resolution with increased overvoltage.

Due to their ready availability, this thesis project uses a Hamamatsu VUV4 model S13371-6050CQ SiPM, illustrated in Fig. 3-5 along with several other VUV4 models. Its key structural, electrical and optical properties are summarized in Table 3-3. The discrepancy in PDEs highlighted there is unlikely to be accounted for by Hamamatsu and nEXO’s different device temperatures during testing: recently published results show a weak dependence of PDE on temperature [59, 60].

PDE does vary with overvoltage and wavelength, however. Fig. 3-6a is a representative example of 13371-6050CQ SiPMs’ photodetection efficiency at and around the LXe scintillation wavelength; all overvoltages produce similar results for this SiPM model. Fig. 3-6b, in the same spectral range, compares PDE measurements from another VUV4 model to 2019 results where specifications were not met. Whether Hamamatsu VUV4s meet specifications may come down to nonuniformity between devices, as those results showed a large spread in PDE — or previous results may have neglected PDE degradation due to exposure to humidity or device degradation.

Finally, Fig. 3-7 shows PDE varying with overvoltage close to 175 nm. At large V_{OV} ($\gtrsim 6$



(a) $V_{OV} = 4$ V. TRIUMF measurements, from 2022: at 163K, with ~ 4 nm FWHM wavelength uncertainty. IHEP, 2022: 300K, ~ 2 nm FWHM wavelength uncertainty. Error bars account for statistical and systematic uncertainty. (b) $V_{OV} = 6$ V. TRIUMF measurements (233K, 2019) show VUV4s failing to meet $> 15\%$ PDE specifications whereas IHEP (300K, 2022) measurements show success over the full range of tested wavelengths.

Figure 3-6: PDE as a function of the wavelength for Hamamatsu VUV4 SiPMs. The legend indicates the type of device and the institution (TR = TRIUMF, IHEP = Institute of High Energy Physics). Note the different scales. Measurement temperatures differ between IHEP and TRIUMF data but are not expected to significantly impact PDE. From [47].

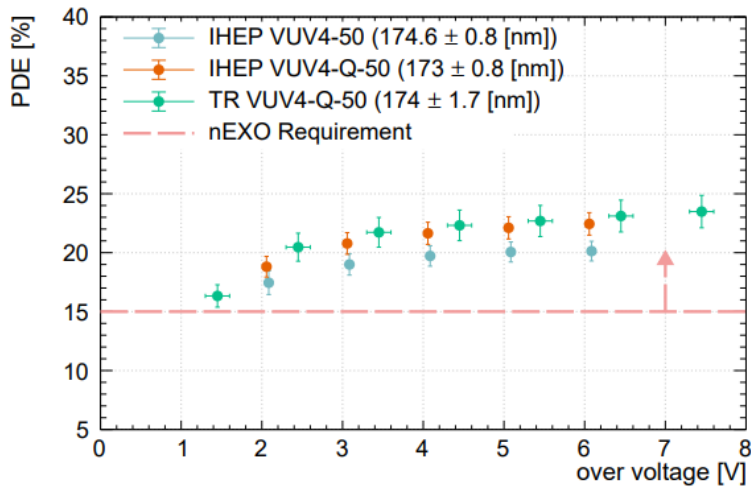


Figure 3-7: Measurements of the PDE at 175 nm as a function of V_{OV} for Hamamatsu VUV4 SiPMs. IHEP and TRIUMF measurements are respectively at 300 K with ~ 2 nm FWHM and at 163 K with ~ 4 nm FWHM. The device exceeds the nEXO PDE requirement of 15%, highlighted by the dashed line. From [47].

Parameter	Value
Structural	
Effective photosensitive area	$5.95 \times 5.85 \text{ mm}^2$
SPAD (pixel) size	$50 \times 50 \text{ }\mu\text{m}^2$
Number of pixels per channel	13,923
Number of channels	4
Electrical and optical	
V_{BD}	$53 \pm 5 \text{ V}$
Recommended V_{OV}	4 V
Gain	2.55×10^6
Spectral response range	155 – 900 nm
CAF	$0.24 \pm 0.04^\dagger$
Dark noise rate	$0.35 \pm 0.01 \text{ Hz/mm}^{2\dagger}$
PDE at 175 nm	24%
	$20.5 \pm 1.1\%^\dagger$

Table 3-3: Structural, electrical and optical properties of the Hamamatsu VUV4 S13371-6050CQ series [61]. Values marked by a † (CAF, dark noise rate, PDE) are from the latest nEXO publication [47] and were taken at 163K and $V_{\text{OV}} = 3 \text{ V}$; other values are from the product flyer [61] and were taken at 25°C. SPAD size will be of particular importance in the following chapters.

V), the PDE is, within uncertainty, independent of overvoltage, which facilitates comparisons like in Fig. 3-6b.

In sum, recent studies show Hamamatsu VUV4s broadly meeting nEXO requirements, including PDE, dark noise rate, CAF rate, and overvoltage range. Regardless of the choice of SiPM vendor, between Hamamatsu and FBK, the devices to be used in the experiment must first be prototyped and tested in order to ensure that they meet selection criteria, notably PDE device-to-device uniformity requirements. In particular, prior to assembly, nEXO will assess PDE uniformity among SiPMs and reject devices whose PDE at 175 nm is either [50]:

- more than 30% below the production run average, or
- more than 2.5σ away from the production run average.

Because device uniformity minimizes testing requirements and prevents bottlenecks, the need for high uniformity ties into a more general preoccupation with testing efficiency in production: at scale, tests must be precise without delaying production.

4 The Optical Rail System

nEXO’s projected scintillation detection capabilities rely on a large photo-coverage area of SiPMs, which requires precision testing. In turn, testing these large-area SiPM modules after integration requires a high throughput and quick turnaround between tile deployment. An Environmental Test Stand (ETS), described elsewhere [62] and currently in operation, facilitates precision testing of integrated tiles by allowing batch measurements of $\lesssim 150$ cm² of SiPMs in vacuum conditions and at nEXO operating temperatures of 168 K with sub-milliKelvin stability. Although it is useful for some measurements to test all the SiPMs the ETS can contain at once, it is also necessary to test individual SiPMs within each batch, and, for higher granularity, individual SPADs within a SiPM. This motivates the creation of an Optical Rail System (ORS) for spatially resolved laser scanning with optics and motion control precision below SPAD scales in the ETS. The design and use of the ORS are documented in this chapter.

4.1 Overview

The ORS exists in two iterations: one for room-temperature testing (Test-ORS) on an optical table and one atop the ETS (ETS-ORS). The latter was developed in parallel to ETS batch measurements, and was moved to the ETS afterwards. It operates on the same principles as the Test-ORS; the setup and data acquisition are virtually identical. In both cases, the ORS’ main three subsystems are (1) the optics, which focus a beam spot onto the SiPM, (2) the linear stages, which control the beam spot’s motion on the face of the SiPM, and (3) signal processing, which extracts pulses from the SiPM’s raw signal. Fig. 4-1 provides a setup overview of the ORS and how the various elements interact with the control software MIDAS (Maximum Integrated Data Acquisition System) [63].

In the signal processing subsystem, an Arduino-based ISEG power source controlled through a Labview program biases the SiPM in reverse mode via a charge-sensitive pream-

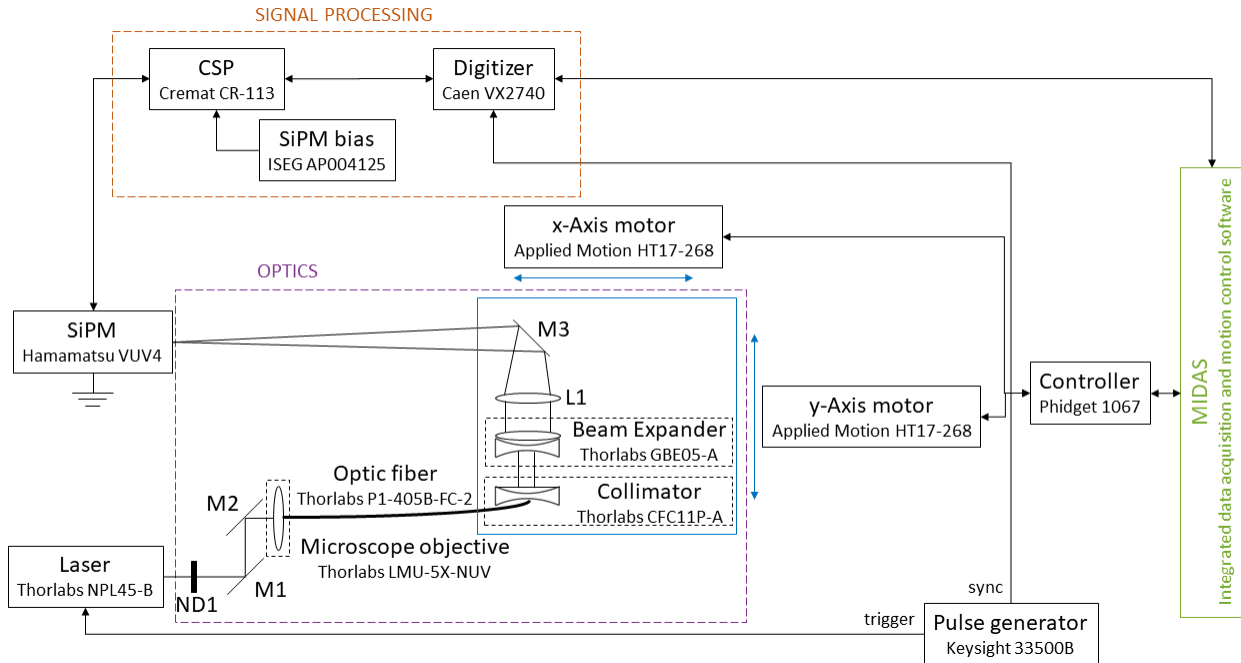


Figure 4-1: Schematic of the ORS setup. Highlighted by coloured boxes are MIDAS (green), the signal processing subsystem (orange), the optics subsystem (purple), and the mobile optics (blue), which are mounted on the movable stage. Model numbers are given for key equipment.

plifier (CSP). Preamplifiers are critical to overall performance, second only to the SiPMs; CSPs, in particular, are typically used in pulse detection circuitry due to their high stability, low noise, and stable gain. The stripped down design of a CSP is shown in Fig. 4-2 [64]. Here, the sub-microsecond pulse the SiPM produces upon light detection is fed to the CSP, which integrates the current and generates a voltage signal, V_{out} , whose amplitude is proportional to the charge, and passes it to a digitizer.

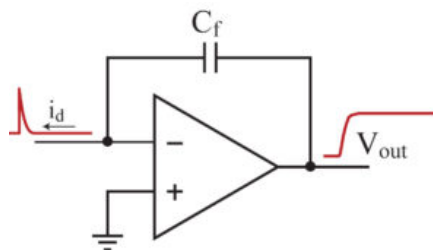


Figure 4-2: Basic schematic of a charge-sensitive preamplifier. The feedback capacitor C_f , drawn above the operational amplifier, converts the current from the detector, i_d , into output voltage V_{out} such that the gain of the preamplifier is $1/C_f$. From [64].

The optics subsystem focuses a laser beam onto SiPMs such that the beam spot diameter is on the order of the size of a SPAD. We use a 450 nm-wavelength laser instead of 175 nm, driven by practical concerns such as the unavailability of commercial 175-nm lasers and the ease of aligning a visible laser. Furthermore, wavelength has no bearing on this thesis project’s demonstration of ORS capabilities. The laser is triggered using a pulse generator; a synchronized trigger is sent to the digitizer for data collection. A microscope objective focuses the beam into an optical fiber, which connects to the mobile optics highlighted in Fig. 4-1. The mobile optics rest atop the linear stage and their motion sweeps the beam spot across the SiPMs. The mirrors are used for alignment. The values of the optics components are provided in Table 4-5. Fig. 4-3 shows a photograph of the optics and the motors for the Test-ORS and Fig. 4-4, for the ETS-ORS.

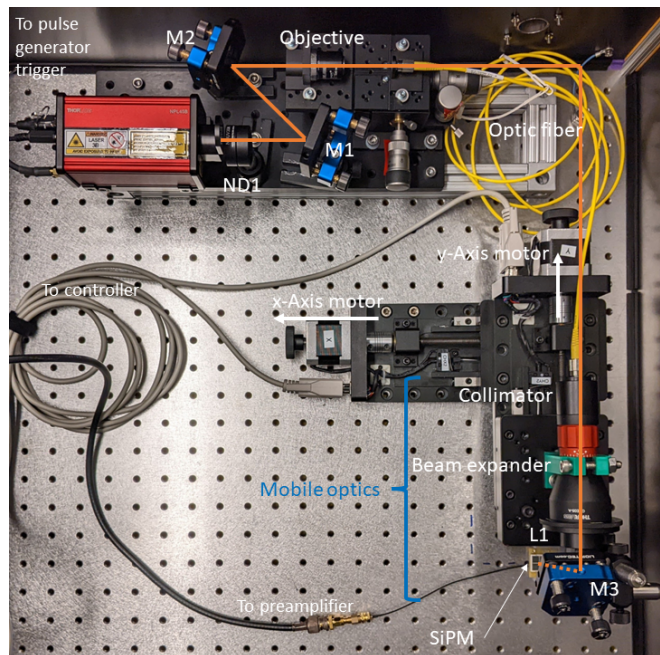
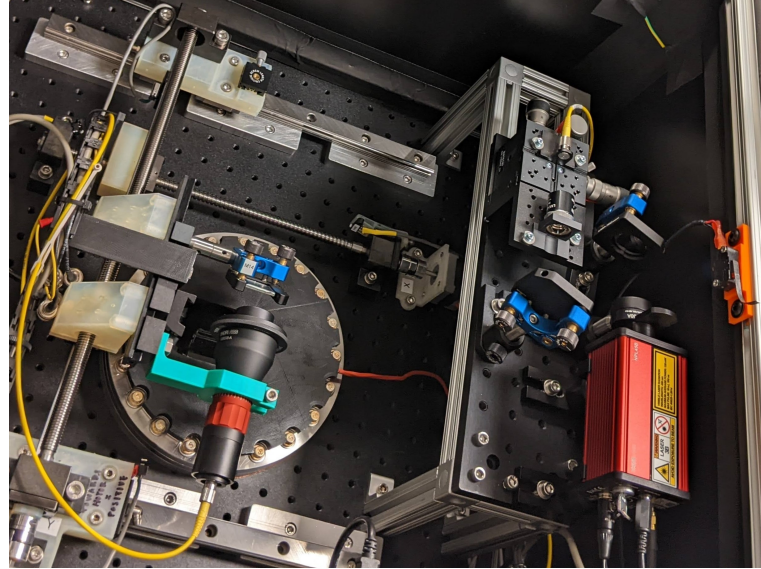


Figure 4-3: Photos of the optics and motors in the Test-ORS. In white: key elements from Fig. 4-1; in orange: the optical path; in blue: the mobile optics, also highlighted in blue in Fig. 4-1. Arrows indicate the negative direction of motion (i.e., moving the stage towards the motor).

The two-dimensional linear stage is composed of one motor each in the x and y directions, with limit switches at extremities to prevent overshooting the range of motion. Both



(a) A mirror reflects the beam onto the SiPM located inside the ETS cryostat, which permits testing at cryogenic temperatures. A single SiPM is visible inside the chamber.



(b) Overview of the ETS-ORS, located within the dark box above the ETS. Putting the optics on a shelf above the x-axis motor has the dual benefit of fitting them within the shared, constrained space of the dark box, and allows most of the optics to be moved to and from the Test-ORS without realignment.

Figure 4-4: Photos of the optics and linear stage in the ETS-ORS.

iterations of the ORS use the same model of motors: two-phase step motors wired in parallel [65]. The motors' position, velocity, and acceleration are set through controllers which receive their instructions from Python scripts and commands [66] developed off of libraries available online [67]. These Python tools may be user-controlled for custom input, or they may be used by MIDAS, notably, to automate the scanning of SiPMs.

MIDAS is a general-purpose, small-scale data acquisition framework intended for experimental physics [63]. In this project, MIDAS combines the stage axes' motion control with the acquisition of SiPM signal data. The cycles of motion and data acquisition required to scan a SiPM are therefore automated; the steps of a scan are illustrated in Fig. 4-5. The resulting data are stored as ROOT files [68], and a dedicated HTTP server enables experiment control through a browser.

MIDAS receives as input a Python-generated map of stop points: locations where the linear stage must pause for data collection. MIDAS sends the command to go to the first

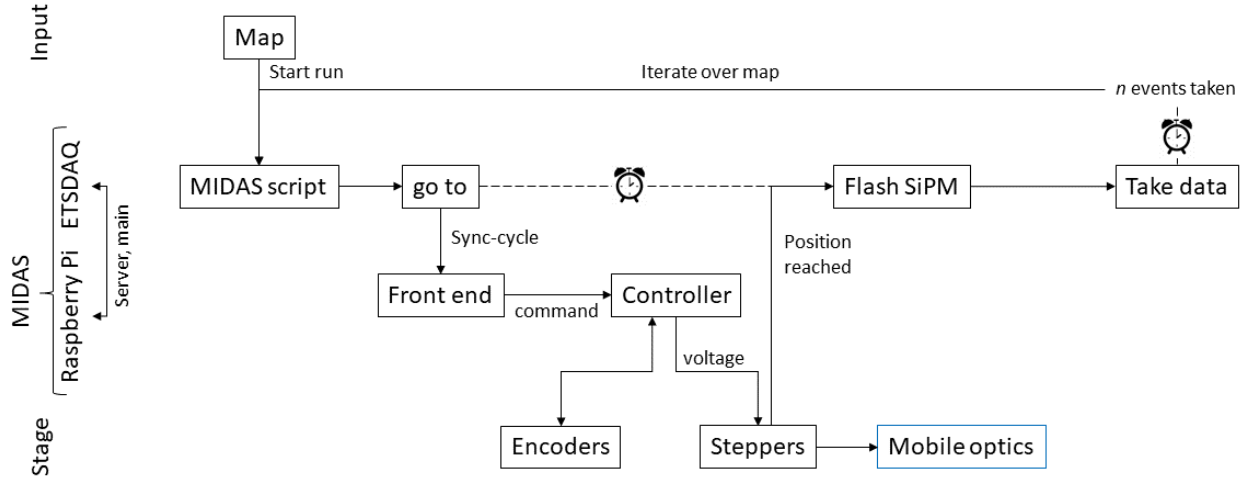


Figure 4-5: Conceptual flow chart of the interactions and commands forming a scan cycle. MIDAS sends commands to the stepper motors’ controllers with a sync-cycle of ~ 200 ms; once the map position is reached, it gathers the data for n events of the SiPM being flashed by the laser before iterating. Mobile optics are shown in Fig. 4-1.

stop point through a front end installed on a Raspberry Pi, which transmits the motion to the stepper motors’ controller. The stepper motors displace the mobile optics, which moves the beam spot across the SiPM surface. Once the position is reached, MIDAS waits n events or pulses, as prompted by the pulse generator’s sync channel, and gathers the data before moving on to the next stop point. Iterating over all the points in the input map completes the scan.

Fast waveform analysis of the resulting data is performed by MERCI [69], a C++ based online/offline modular analyzer for MIDAS-based experiments, specializing in fast waveform analysis for SiPMs and PMTs. MERCI output and ORS positional data are saved jointly in the ROOT files to allow correlation; this is the basis of the analysis presented in Chapter 5.

4.2 Characterization of the Optical Rail System

The key functionality requirements for the ORS concern, first, the precision and accuracy of motion control with regard to SPAD size (typically $\sim 50 - 70 \mu\text{m}$ per side, but $50 \mu\text{m}$ for the Hamamatsu VUV4s used in this project per Table 3-3), and, second, the beam spot size, which ideally is on the order of a SPAD.

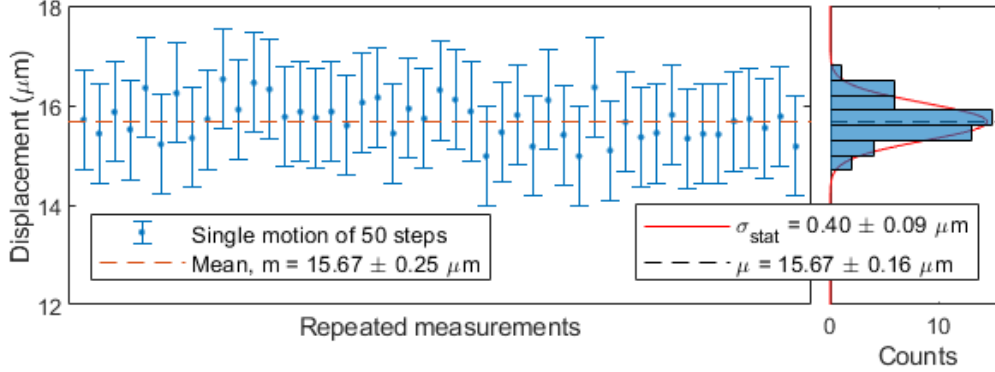


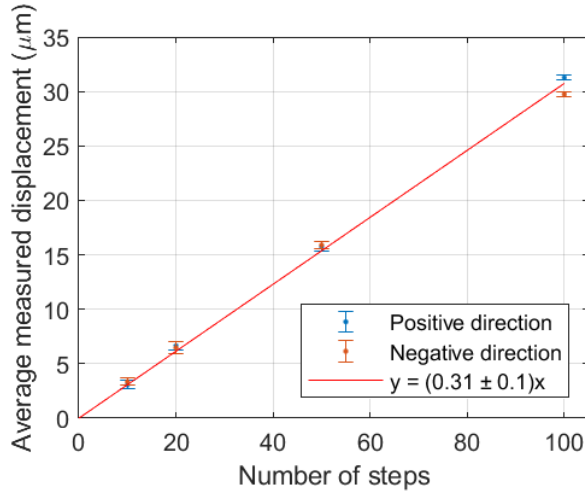
Figure 4-6: Displacement consistency of the least consistent calibration sample at \sim SPAD scale along the Test-ORS x-axis at a given step size of 50 steps. Error bars on the left panel are the systematic uncertainty of the calipers used to measure displacement. All systematic uncertainties overlap the fit value and the arithmetic mean, m , agrees with the center of the Gaussian fit, μ . The right panel shows that the standard deviation of the sample is $\sigma = (0.40 \pm 0.09) \mu\text{m}$, such that over a raster scan, the total expected error is below one SPAD.

4.2.1 Linear Stage: Motion Control and Calibration

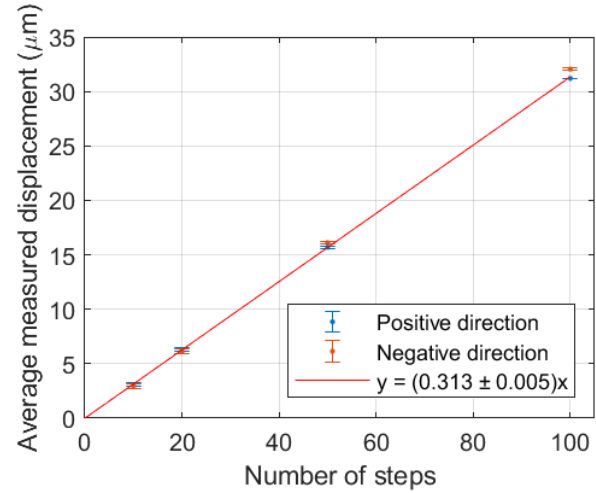
In order to interface with commercial stepper motors, motion commands are issued from the Python scripts in terms of steps rather than distance or displacement. This in turn requires a precision calibration of the step-to-displacement conversion on scales ranging from ~ 10 cm to $\sim 10 \mu\text{m}$, where larger scales correspond to the size of an axis and are needed in homing and SiPM-finding protocols; the smaller scales are used in SPAD-wise scanning and testing. For these high-granularity scans, scanning across the full width of a SiPM, the accumulated displacement error along one axis must be inferior to the size of a SPAD to ensure each SPAD is tested individually.

In order to study the stepper motor's consistency, repeated displacements by 50 steps were issued and the traveled distance was measured using a caliper. The results are shown in Fig. 4-6, which highlights the stepper motors' consistency at the \sim SPAD scale. The caliper's uncertainty makes up the displayed systematic error. Taking the standard deviation, denoted σ_{stat} , as a gauge of statistical fluctuations, the data in Fig. 4-6 has the largest statistical fluctuations of all calibration samples at this scale. Assuming that $\sim \mathcal{O}(10^2)$

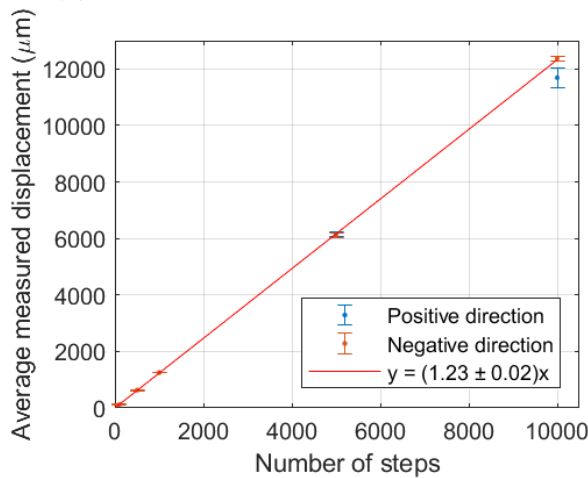
SPAD-scale displacements are required to scan across a full width of a SiPM, the total cumulated error is below the size of a SPAD. Thus, motion accuracy over a SiPM raster scan exceeds performance requirements.



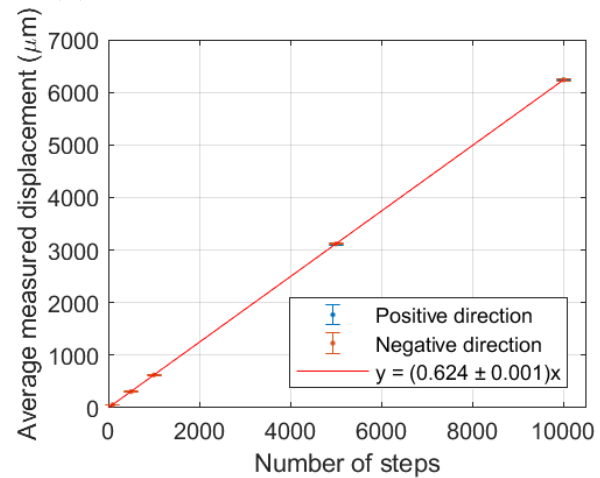
(a) Test-ORS x-axis. $\chi^2 = 7.48$ for 3 dof.



(b) Test-ORS y-axis. $\chi^2 = 20.76$ for 3 dof.



(c) ETS-ORS x-axis. $\chi^2 = 6.11$ for 4 dof.



(d) ETS-ORS y-axis. $\chi^2 = 0.864$ for 4 dof.

Figure 4-7: Calibration results for the ETS-ORS and Test-ORS. As indicated in Fig. 4-4, positive direction indicates displacement of the stage away from the motor and negative direction, towards the motor. Error bars represent the standard deviation on each sample, σ_{stat} , such as the sample from Fig. 4-6. A weighted mean of the data in both directions yields the displayed linear least-squares fits with a forced null zero-intercept; values are displayed in Table 4-4. Differences in slopes reflect differences in the pitch of each axis' the ball screw, which converts rotation into linear motion.

Data from Fig. 4-6 is averaged to produce one data point in Fig. 4-7, where the error bars are σ_{stat} . As a further consistency check, measurements were made in both directions

of motion. Figs. 4-7a and 4-7b show calibration of the Test-ORS axes in the $\sim 100 - 10 \mu\text{m}$ range, and Figs. 4-7c and 4-7d show larger-scale calibration for the ETS-ORS axes down to $\sim 100 \mu\text{m}$.

The linearity of displacement with the number of steps testifies to the precision of the stepper motors at every scale, for all axis motors. Furthermore, step-to- μm conversion factors, a , can be extracted from the slope of the fit. As a check, we initially calculated conversion factors separately in the positive and negative directions (towards and away from the motors). Results overlapped and for simplicity, we used a weighted mean of both directions as a -values. Slopes also match well within error whether the y-intercept is forced to 0 or not, as shown in Table 4-4. For simplicity and uniformity, those with forced null y-intercept were used.

Slope values vary between the ETS-ORS and the Test-ORS and among ETS-ORS axes in Fig. 4-7 and Table 4-4 because of differences in the axes' ball screws, which translate the rotational motion of the stepper motor into linear motion for the stage. The ratio of the slopes, a_x/a_y , should match the ratio of ball screw pitches; Table 4-4 shows agreement between measured and theoretical values.

Thus characterization of the ORS' linear stage subsystem shows that its motion is reliable and predictable over scales from $\sim 10 \text{ cm}$ to $\sim 10 \mu\text{m}$, and its consistency at SPAD scales enables SPAD-wise scanning.

4.2.2 Optics: Beam Spot Size

Per [70], the beam waist ω_0 of a Gaussian beam can be calculated from the beam diameter before the focusing lens using

$$\omega_0 = \frac{2\lambda f}{\pi d}, \quad (9)$$

where λ is the wavelength, d is the input beam diameter, and f is the focal length of lens L1 from Fig. 4-1. If the beam is Gaussian, ω_0 corresponds to the distance between points

Test-ORS				
	<i>x</i> -axis	<i>y</i> -axis	a_x/a_y (meas)	a_x/a_y (theo)
$l = as$				
a ($\mu\text{m}/\text{step}$)	0.31 ± 0.01	0.31 ± 0.01	0.99 ± 0.04	1
$l = as + b$				
a ($\mu\text{m}/\text{step}$)	0.30 ± 0.02	0.31 ± 0.01	0.96 ± 0.10	1
b (μm)	0.5 ± 1.1	0 ± 1	-	-
ETS-ORS				
	<i>x</i> -axis	<i>y</i> -axis	a_x/a_y (meas)	a_x/a_y (theo)
$l = as$				
a ($\mu\text{m}/\text{step}$)	1.23 ± 0.02	0.624 ± 0.001	1.97 ± 0.04	2
$l = as + b$				
a ($\mu\text{m}/\text{step}$)	1.23 ± 0.03	0.624 ± 0.001	1.97 ± 0.05	2
b (μm)	1 ± 51	-3 ± 2	-	-

Table 4-4: Conversion factors from motor step size s to measured displacement l , extracted from the calibration. For both axes, whether the y-intercept is fixed at 0 or not, slopes match well within error. The ratio of slopes for the two axes, a_x/a_y , yields the value expected from their different ball screw pitches.

whose intensity is $1/e^2$ of the peak intensity. This yields a larger diameter than the full width half-maximum (FWHM) intensity, the other commonly accepted method of measuring beam spot size, since $\text{FWHM} = \omega_0 \sqrt{(\ln 2)/2}$. Eq. 9 is therefore the more stringent requirement for the theoretical minimal beam spot diameter.

Fig. 4-8 illustrates the computation of experimentally achieved beam diameters. The beam spot in Fig. 4-8 is not the smallest achieved — that is listed in Table 4-5 — but it displays the analysis better. To determine the size of the beam spot, we use the Test-ORS setup illustrated in Fig. 4-3 and the ETS-ORS setup illustrated in Fig. 4-4. Only the optics subsystem is of interest. The beam spot is photographed using a CMOS camera ([Thorlabs CS165CU](#)) of known pixel size located at the focal point. We locate the beam spot’s peak intensity in the photograph by identifying the pixel of highest cumulative RGB intensity, and we trace $1/e^2$ intensity contour lines (illustrated in red in Fig. 4-8) around it by comparing cumulative RGB intensity of each pixel to that of the pixel with the highest intensity. Using the known pixel size, these contour lines are fitted with a tilted ellipse using code from [71], accounting for the possibility of an imperfectly circular beam whose greatest diameter may

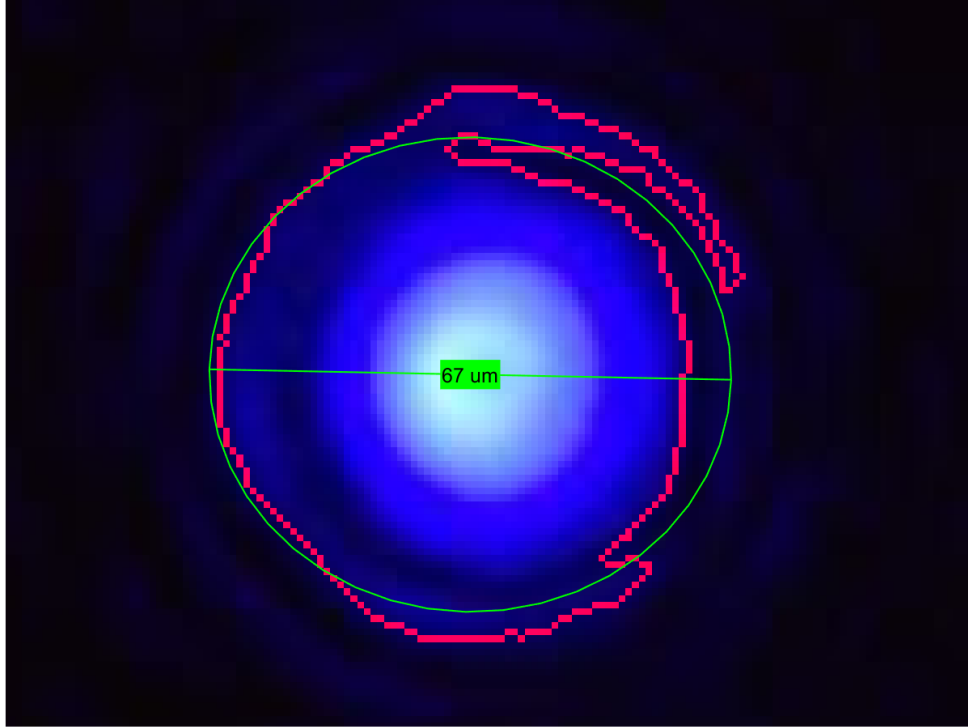


Figure 4-8: Beam spot and elliptical fit to determine $1/e^2$ diameter. In red: $1/e^2$ intensity from photo RGB values. In green: least squares fitted ellipse [71]; note the light tilt, which makes the ellipse span its largest diameter. The ellipse-fitting code is fed distances in microns rather than in pixels; the conversion is known from the camera’s pixel size. The beam spot’s size is taken to be the length of the semi-major axis of the fitted ellipse. Photo taken on a Thorlabs CS165 Series CMOS camera, which has $3.45\ \mu\text{m} \times 3.45\ \mu\text{m}$ pixels. This is not the smallest beam spot achieved in either iteration of the ORS.

lie in any direction, as the beam spot may skew from the (arbitrary) photo axes. The ellipse’s semi-major axis is taken as the beam diameter.

Table 4-5 compares theoretical and achieved values of ω_0 in both ORS iterations given $\lambda = 450\ \text{nm}$ and their respective focal lengths f . In both cases, the theoretical value is an order of magnitude below SPAD scale, which satisfies the requirements of SPAD-wise scanning. Diameters achieved so far are an order of magnitude above the theoretical minimum. For the Test-ORS, the experimentally achieved diameter remains below SPAD size and allows for SPAD-wise testing; not for the ETS-ORS, however. This is discussed further in the outlook in Chapter 5.

In sum, the optics in the ETS-ORS require fine-tuning, but motor control in both ORS

	Test-ORS	ETS-ORS
f_{L1} (cm)	15	25
ω_0 ($1/e^2$, μm)		
Theoretical (Eq. 9)	5.4	9.0
Achieved	44 ± 5	63 ± 6

Table 4-5: Differing values in the optics subsystems of the Test-ORS and ETS-ORS. The ETS-ORS requires a longer focal length due to the distance between the window and the SiPMs, which was set independently of this thesis project by constraints on the ETS design. A SPAD has sides of $50 \mu\text{m}$. The uncertainties on achieved ω_0 result from the error propagation of an initial error of one pixel, $3.45 \mu\text{m}$.

iterations exceeds the $50 \mu\text{m}$ requirement set by SPAD dimensions, and the beam spot sizes achieved in the Test-ORS allow for SPAD-wise testing of Hamamatsu VUV4 SiPMs. Early results from the Test-ORS are presented in Chapter 5.

5 Results from Commissioning

In this chapter, we present results from scanning a beam spot in raster grids over the surface of Hamamatsu VUV4 SiPMs with the Test-ORS. First, we outline the analysis steps which produce a raster scan; the intermediary results showcase the capabilities of the ORS. Then, we use SPAD-scale scans to evaluate the uniformity of SPAD response and relative PDE. The Test-ORS takes room temperature measurements (~ 293 K), and for these temperatures, we find a dark rate of $\sim 10^5$ Hz, but as mentioned in Chapter 4, data collection is synchronized to the laser trigger.

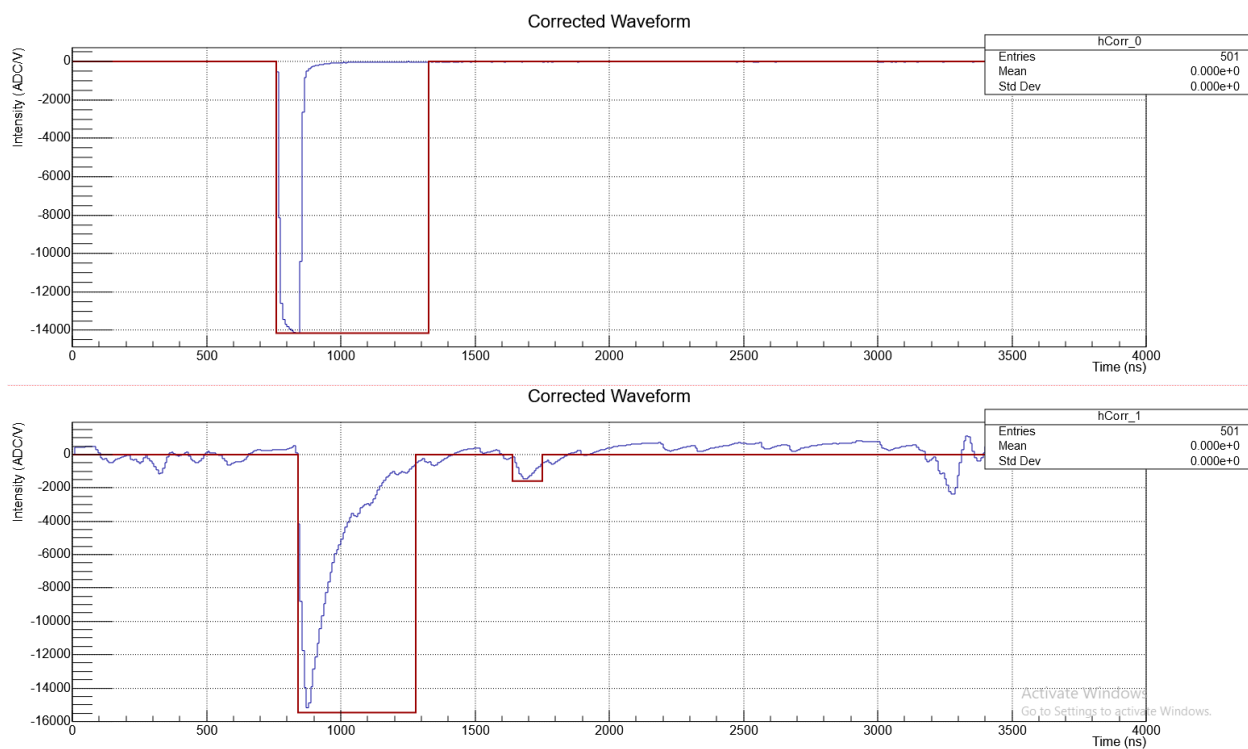


Figure 5-1: Typical pulses: signal intensity as a function of time for the laser trigger (top) and SiPM signal (bottom), as displayed by MERCI’s online frontend during live analysis. In blue: waveforms, in red: pulses identified by MERCI. In the bottom panel, a sub-pulse is flagged as well. Waveforms are baseline corrected: an average baseline level is computed from a pre-trigger sample region, and subtracted from the raw waveform.

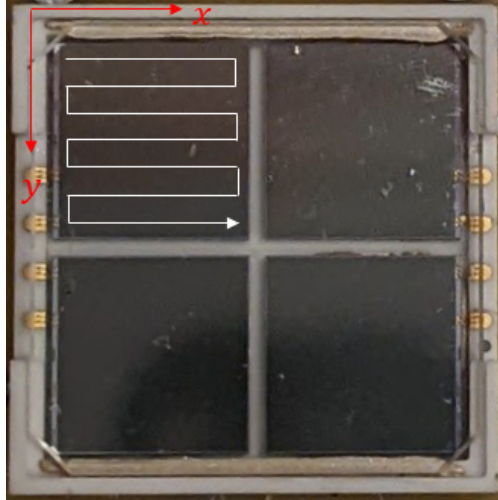


Figure 5-2: Raster scan pattern overlaid in white on a Hamamatsu VUV4 SiPM. In this model, 4 SiPMs form a quad.

5.1 Building a Raster Scan

Generally, raster scans establish control over all ORS moving parts and correlate them. We use all parts and subsystems illustrated in Fig. 4-1, with the beam spot focused to below step size. For initial, coarse scans, a single pulse, or event, consists of $\sim 10^3$ photons. MIDAS records a user-specified number of pulses — here, $n = 200$ pulses per stop point — and therefore laser repetition rate only affects runtime, and can be set arbitrarily (within signal processing capabilities).

MIDAS receives the raw waveform and identifies the pulse; Fig. 5-1 exemplifies the online display during live analysis, with the laser trigger signal and a baseline-corrected SiPM signal overlaid with the identified pulse. Notably, MERCI records timestamps for all pulses and calculates their amplitude A — that is, the value of the pulse peak, assuming a corrected baseline of 0.

At each stop point, the linear stage pauses for data collection, MIDAS waits for n such pulses before moving on to the next, eventually completing a pattern like the one illustrated in Fig. 5-2. This constitutes a raster scan. By correlating MERCI analysis of SiPM signal with the scanner position, we average the amplitudes of all pulses collected at a given stop

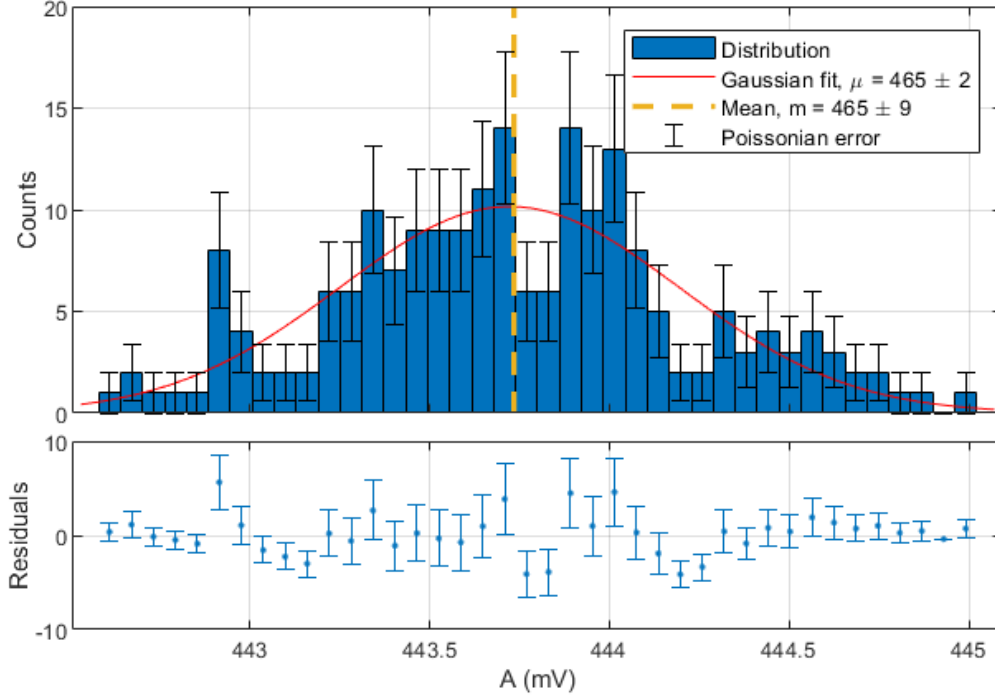


Figure 5-3: Signal amplitude distribution for all pulse events recorded at a single stop point. Error bars reflect the Poisson distribution of the counts. The histogram is fairly Gaussian ($\chi^2 = 34.71$ for 37 dof), with the fit centered at $\mu = (465 \pm 2)$ mV. Given that $\mu \approx m$, the average, we assign the average amplitude to this stop point. This histogram has 200 pulses in total, the lowest number of pulses per stop point taken in this project; agreement between the average and the Gaussian mean is therefore good even for the smallest populations used in this analysis. The ADC voltage in Fig. 5-1 has been converted to mV.

point. Fig. 5-3 justifies the use of averages by highlighting the Gaussian behaviour of multiple pulses: even with relatively few of them, like $n = 200$, the center of the Gaussian agrees with the average. Because the Central Limit Theorem states that the agreement between the mean and the Gaussian should improve with more pulses, the agreement shown in Fig. 5-3, for lower pulse counts, allows us to proceed.

With a single (average) amplitude value A_i at each stop point i , we plot a heatmap. Fig. 5-4 is a coarse raster scan of pulse amplitude, displaying fluctuations rather than absolute values, i.e.:

$$f_i = A_i - \bar{A}, \quad (10)$$

where f is the displayed fluctuation. With absolute values of $A_i \sim 450$ mV (per Fig. 5-3)

and fluctuations of $f_i \sim 1$ mV (per Fig. 5-4), fluctuations show sub-percent uniformity. The clustering of data — A_i averages many photons per pulse, many pulses per stop point, and covers multiple SPADs — may dampen variations.

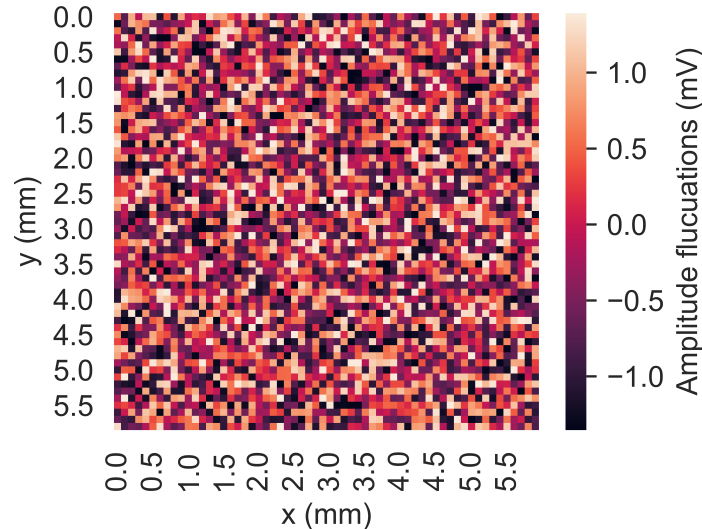


Figure 5-4: Raster scan of a Hamamatsu VUV4 SiPM with a granularity of $100\mu\text{m}$, showing fluctuations in signal amplitude, f_i . Given this step size, pictured squares do not correspond to SPADs. Data was taken on the Test-ORS with an overvoltage of $V_{\text{OV}} = 5$ V and a beam spot of (89 ± 7) μm in diameter.

It should be noted that squares in Fig. 5-4 do not correspond to SPADs or to beam spot size, but to the locations of the stop points. Since the signal is an analog sum of all SPADs, it is impossible to determine which SPADs are firing — hence the importance of fine motor control and good parametrization of the beam spot diameter. SPAD-wise scanning, combined with a beam diameter below SPAD scale, constitute the best assurance that the signal comes from the targeted SPAD.

5.2 SPAD-wise Scans

This section presents results from a partial SiPM scan of four rows of SPADs, where each row was scanned SPAD-wise. We assume SPAD-wise scanning based on the set step size of $50\mu\text{m}$, and on the motion consistency verified in Chapter 4. Motion follows the pattern from Fig. 5-2, but with each scan row beginning outside the SiPM, to avoid missing edge-adjacent

Scan parameter	Value
Pulses per stop point, n	2000
x -step	50 μm
y -step	1000 μm
Number of stop points per row	200
Number of rows	4

Table 5-6: Parameters of the SPAD-wise scan. All these parameters are set by the user in MIDAS. The lines scanned along the x -axis exceed the dimensions of the SiPM to avoid missing SPADs located near the edge. Motion along a row is in the x -direction shown in Fig. 5-2.

SPADs. All results in this subsection are based on a single data run, whose parameters are given in Table 5-6.

Beam Spot Diameter

To determine the beam spot size, we compare the size obtained through imaging with a CMOS camera, as described in Chapter 4, to the size we obtain by deconvolving the Gaussian shape of the beam from the step response at the SiPM edge. In Fig. 5-5, the beam spot moves onto the SiPM: at each stop point, MIDAS records 2000 pulses, and their amplitudes are plotted against the stop point's position along the axis of motion, x . The increase in amplitudes shows the beam spot, initially beyond the edge of the SiPM, moving onto the SiPM.

The beam spot has a Gaussian shape, and the SiPM edge is modeled as a step function, $H(x)$; the convolution of these two is an error function:

$$\exp\left(\frac{-(x - \mu)^2}{2\sigma^2}\right) * H(x) = k \operatorname{erf}\left(\frac{x - \mu}{\sqrt{2}\sigma}\right), \quad (11)$$

where k is a constant. Thus, we deconvolve the best-fit error function to obtain the parameters of the Gaussian beam. Once its standard deviation is known, we calculate the $1/e^2$ diameter of the beam with $\omega_0 = 4\sigma$.

Using signal at both edges of the SiPM from each of the four rows, we obtain a $1/e^2$

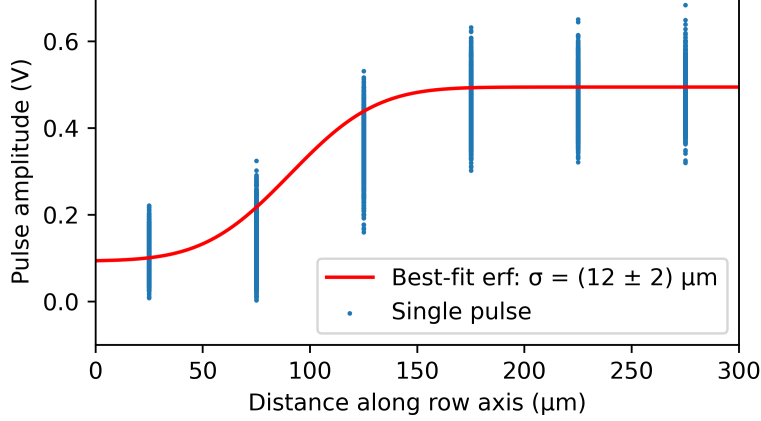


Figure 5-5: Error function fit of the signal at a SiPM edge. As the linear stage moves the beam spot across the SiPM edge with a $50\ \mu\text{m}$ (SPAD-sized) step, 2000 signal pulses are recorded at each location. The Gaussian shape of the beam spot, convolved with the step response at the SiPM edge, yields the error function; a fit on this error function yields the parameters of the Gaussian beam, from which we calculate ω_0 , the $1/e^2$ beam diameter. The fit in this figure gives a beam diameter of $(47 \pm 7)\ \mu\text{m}$. Here, $\chi^2 = 12,206$ for 11,996 dof.

diameter of $(46 \pm 3)\ \mu\text{m}$ for this data run. This agrees with the imaging value of $(48 \pm 5)\ \mu\text{m}$ for the same data run, for a combined diameter of $(\omega_0 = 47 \pm 6)\ \mu\text{m}$. Thus, for this SPAD-wise scan, the laser beam spot is smaller than a SPAD.

SPAD Signal Homogeneity over a Single Scan Row

Having verified the size of the beam spot, we scan it across the face of the SiPM to record pulses at the stop points, set $50\ \mu\text{m}$ apart and presumed to be the SPADs lying along the axis of motion. We take the average pulse amplitude at each stop point, as done for the coarse scan: as before, this is justified by the agreement between the center of the Gaussian distribution with the mean. Fig. 5-6, analogous to Fig. 5-3, exemplifies the strong agreement for high pulse counts.

Fig. 5-7 shows fluctuations in the average pulse amplitudes for one row of SPADs. Some fluctuations, visible as bright lines in Fig. 5-7, exceed the sub-percent uniformity exhibited in the coarser scan of Fig. 5-4 by an order of magnitude. We call these hotspots, and they make up $\sim 1.5\%$ of SPADs. We do not know what causes them; see suggestions on future work in Chapter 6.

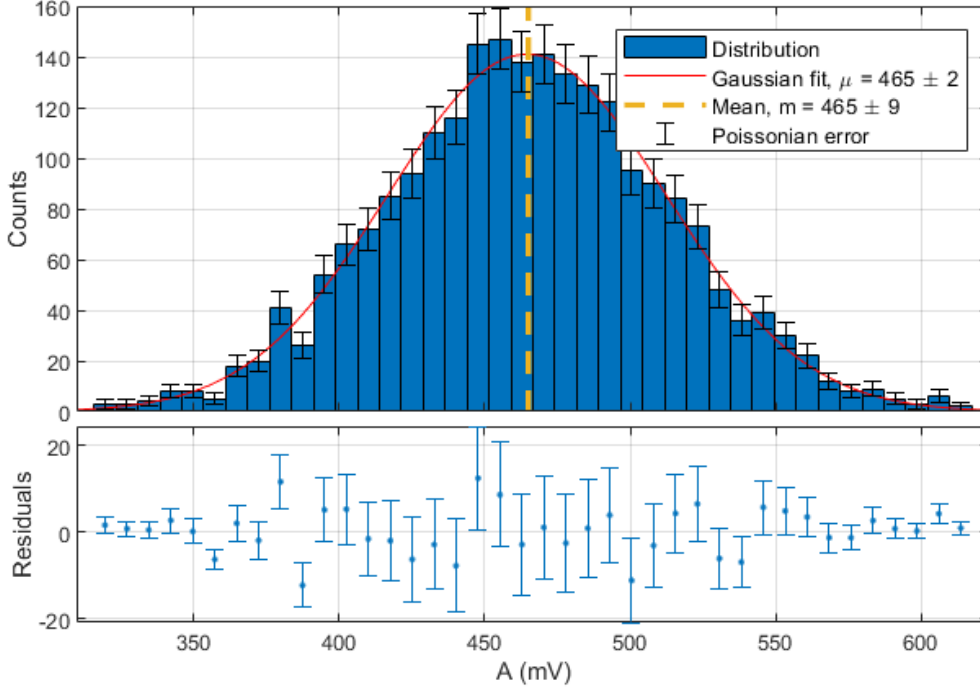


Figure 5-6: Signal amplitude distribution for a single SPAD: the shape is Gaussian ($\chi^2 = 43.68$ for 37 dof), as for the lower pulse count of Fig. 5-3. The arithmetic mean and the center of the Gaussian distribution are identical within significant digits.

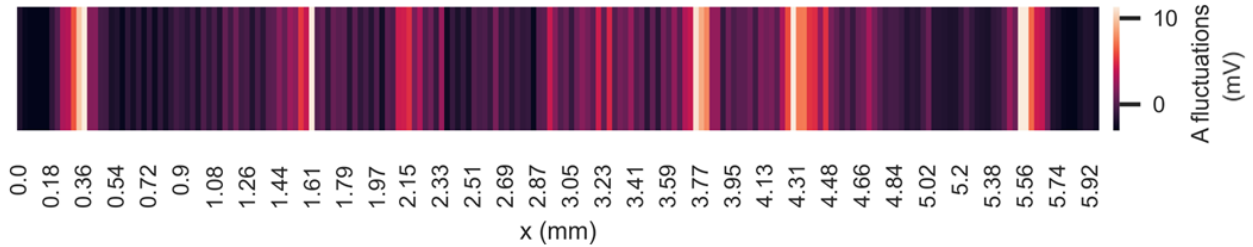


Figure 5-7: Scan of a single row of SPADs ($50 \mu\text{m}$ granularity) on a Hamamatsu VUV4 SiPM. The largest fluctuations (“hotspots”) are an order of magnitude larger than in Fig. 5-4 ($\sim 10 \text{ mV}$); their cause is unknown. Data was taken on the Test-ORS with an overvoltage of $V_{\text{OV}} = 5 \text{ V}$ and a beam spot of $(47 \pm 7) \mu\text{m}$ in diameter.

However, even discounting hotspots, SPAD-wise scans display less homogeneity than coarse scans. Table 5-7 compares the standard deviations, as an indicator of dispersion, of the amplitude fluctuations in the coarse scan, in the SPAD-wise scan, and in the SPAD-wise scan where hotspots have been removed from the dataset using a modified Z-score exclusion method [72]. Table 5-7 shows that hotspots increase the dispersion in fluctuations, but it also indicates that even *without* hotspots, response fluctuates significantly more in the SPAD-

Standard deviation of fluctuations	
σ_{f_i} (mV)	
Coarse scan	0.93 ± 0.09
SPAD-wise scan	
With hotspots	3.6 ± 0.2
Without hotspots	2.8 ± 0.2

Table 5-7: Standard deviation of signal amplitude fluctuations for the coarse scan, and for the SPAD-wise scan with and without hotspots. Hotspots introduce high statistical variation, driving down the homogeneity of the SPAD-wise scan. However, even without hotspots, the SPAD-wise scan has a higher dispersion.

wise scan than in the coarse scan. As suggested earlier, the uniformity of coarse scans may have been driven down by the fact that they average over many SPADs.

SPAD Signal Homogeneity over Multiple Scan Rows

Over all four rows of SPADs taken consecutively, another trend emerges: pulse amplitude increases, as highlighted by the diverging linear fits in Fig. 5-8. The linearity with time is noteworthy, being unlikely to reflect SiPM response. It is also unlikely to stem from temperature-dependent effects in the signal processing electronics, as they had been turned on for other runs for many hours before the run presented here. However, MIDAS is able to record the temperature of the digitizer; temperature stability monitoring could be implemented to rule this out. Unlike the signal processing electronics, however, the laser was turned off between runs, and the higher slope of the on-SiPM signal (as opposed to off-SiPM signal, both shown in Fig. 5-8) may suggest that the laser beam intensity increases with time. Laser stability could be quantified by recalibration, such as scanning the same row twice over, without any modifications to the setup. Alternatively, the laser beam could be split into two, as done in [73–75], so that one arm may be monitored by a calibrated photodetector for long-term variations in intensity.

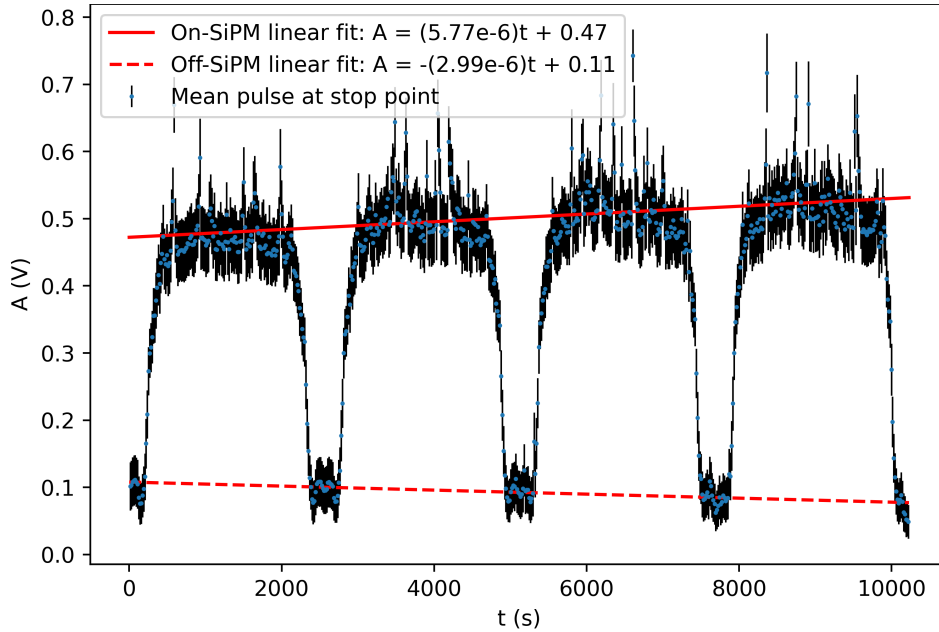


Figure 5-8: Mean pulse amplitude versus time for all scan rows, consecutively. Each point (blue) is the mean amplitude at that stop point; error bars (black) are the standard deviation. Amplitude is plotted against time to emphasize the trend — analysis ensures that no two consecutive data points are at the same location. The four rows are clearly distinguished, as signal drops when the beam reaches the edge, as in Fig. 5-5. The diverging linear trends show that the signal received when the beam spot is on the SiPM (full red line) consistently increases, while the signal received when the beam spot is beyond the SiPM edge (dashed red line) consistently decreases. Only data points which are calculated to have the beam spot’s full $1/e^2$ diameter on or off the SiPM contribute to the fits; rising and falling flanks are not considered.

Relative Photon Detection Efficiency of SPADs

To evaluate SPAD performance, we calculate the relative PDE at each stop point — still assuming, by virtue of the $50\ \mu\text{m}$ step size, that each corresponds to a SPAD. Borrowing the criteria listed at the end of Chapter 3 and applying them to SPADs rather than to SiPMs, we compute the fraction of SPADs which are more than 30% below, or more than 2.5σ away from, the run average. A SiPM may still be good if it has outlying SPADs; the nEXO criteria apply on the SiPM level only. Although we borrow them here, our analysis does not determine the goodness or badness of a SiPM. Owing to the linear increase illustrated in Fig. 5-8, PDE is calculated separately for each row, relative to its central SPAD (or the closest adjacent non-hotspot).

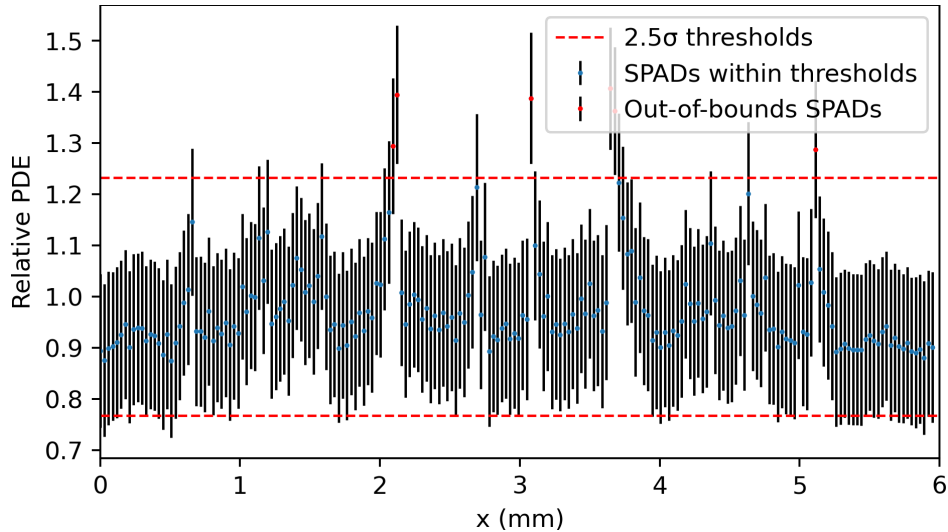


Figure 5-9: Relative PDE of a row of SPADs, with some SPADs excluded by the PDE acceptance criteria laid out in Chapter 3. Error bars account for statistical error, propagated as data was normalized. Here, the 2.5σ constraints were more stringent, and the threshold at 30% below run average is not shown. Here, 3.1% of the SPADs display performance beyond accepted thresholds.

Fig. 5-9 shows this variation in SPAD performance and highlights those out of bounds for one row. It also shows spikes: some out-of-bounds SPADs (but not all) are preceded by a gradual increase in PDE, or followed by a gradual decrease in PDE. These spikes are present in all rows, and no pattern governing which way they skew has been found. Their cause is unknown and will require further investigation.

Further, in all four rows, the rejected SPADs were all *above* rejection thresholds, and account for between 2.7% and 5% of SPADs. SPAD-wise scanning of entire SiPMs, rather than four rows as done for these commissioning results, could examine whether the 2.7%–5% rejection rates found here are generalized to entire SiPMs — at least, the Hamamatsu VUV4s available for testing.

In general, while results from commissioning display the capabilities of the ORS to scan a laser spot across a SiPM surface and gather data, they also raise questions concerning systematic effects and uncertainties. Next steps, including but not limited to those suggested in Chapter 6, will be a thorough investigation on these points.

6 Conclusion and Outlook

The neutrino sector is a promising area for new physics, and the proposed nEXO experiment aims to investigate the nature of the neutrino by searching for neutrinoless double beta decay [7, 22]. Testing nEXO’s large number of silicon photomultipliers on reasonable timescales and at operating temperatures requires an automated approach and high throughput. An environmental test stand for large-area, cryogenic-temperature testing of SiPMs has been developed elsewhere [62].

This thesis presents the design and assembly of a complementary Optical Rail System (ORS) combining optics and motion control for precision scanning of multiple SiPMs. Two ORS were built, one operating at room temperature (Test-ORS) and the other adopted for cryogenic testing (ETS-ORS). Both are shown to operate with motion control beyond the stated objective of 50 μm and both may reach beam spot sizes under 50 μm , though this has only been achieved in the Test-ORS, which was used for commissioning results. Commissioning results, also presented in this thesis, demonstrate the building of coarse or fine raster scans to evaluate SiPM performance. They raise questions concerning (a) hotspots, pixels with outstandingly high response, (b) linear increases in pixel response throughout the scanning process, and (c) the photon detection efficiencies of pixels — all of which will require further investigation.

Future improvements to either ORS may include adding a beam splitter and a calibration photodetector to adjust for varying laser intensity. Going forward, further tests will be carried out with the ETS-ORS at cryogenic temperatures, and the analysis processes created for this thesis will help develop strategies towards larger-scale testing of assembled staves for the nEXO project.

References

- [1] F. Reines and C. Cowan. “The Reines-Cowan experiments: Detecting the Poltergeist”. In: *Los Alamos Sci.* 25 (1997), pp. 4–27.
- [2] *The Nobel Prize in Physics 1995*. URL: <https://www.nobelprize.org/prizes/physics/1995/summary/>. (Accessed: 06.08.2022).
- [3] Bruce T. Cleveland et al. “Measurement of the Solar Electron Neutrino Flux with the Homestake Chlorine Detector”. In: *The Astrophysical Journal* 496.1 (1998), p. 505.
- [4] H. A. Bethe. “Energy Production in Stars”. In: *Physical Review* 55 (5 1939), pp. 434–456.
- [5] John N. Bahcall. “Neutrinos from the Sun”. In: *Scientific American* 221.1 (1969), pp. 28–37.
- [6] *The Nobel Prize in Physics 2002*. URL: <https://www.nobelprize.org/prizes/physics/2002/summary/>.
- [7] M. Agostini et al. “Probing Majorana neutrinos with double- β decay”. In: *Science* 365.6460 (2019), pp. 1445–1448.
- [8] Q. R. Ahmad et al. “Direct Evidence for Neutrino Flavor Transformation from Neutral-Current Interactions in the Sudbury Neutrino Observatory”. In: *Physical Review Letters* 89 (1 2002), p. 011301.
- [9] *The Nobel Prize in Physics 2015*. URL: <https://www.nobelprize.org/prizes/physics/2015/summary/>. (Accessed: 16.09.2022).
- [10] Z. Maki, M. Nakagawa, and S. Sakata. “Remarks on the Unified Model of Elementary Particles”. In: *Progress of Theoretical Physics* 28.5 (1962), pp. 870–880.
- [11] Joseph A. Formaggio, André Luiz C. de Gouvêa, and R.G. Hamish Robertson. “Direct measurements of neutrino mass”. In: *Physics Reports* 914 (2021), pp. 1–54.

- [12] P.A. Zyla et al. “Review of Particle Physics”. In: *Progress of Theoretical and Experimental Physics* 2020.8 (2020). And 2021 update, p. 083C01.
- [13] P.F. de Salas et al. “Status of neutrino oscillations 2018: 3σ hint for normal mass ordering and improved CP sensitivity”. In: *Physics Letters B* 782 (2018), pp. 633–640.
- [14] N. Aghanim et al. “Planck 2018 results - VI. Cosmological parameters”. In: *Astronomy & Astrophysics* 641 (2020).
- [15] C. Adams et al. *Neutrinoless Double Beta Decay*. 2022.
- [16] M. Aker et al. “Direct neutrino-mass measurement with sub-electronvolt sensitivity”. In: *Nature Physics* 18 (2022), pp. 160–166.
- [17] Mark Thomson. *Modern particle physics*. New York: Cambridge University Press, 2013. ISBN: 978-1-107-03426-6.
- [18] K. S. Babu and V. S. Mathur. “Radiatively induced seesaw mechanism for neutrino masses”. In: *Physical Review D* 38 (11 1988), pp. 3550–3553.
- [19] M. Goeppert-Mayer. “Double Beta-Disintegration”. In: *Physical Review* 48 (6 1935), pp. 512–516.
- [20] Petr Vogel. “Neutrinoless double beta decay”. In: *AIP Conference Proceedings*. AIP, 2006.
- [21] T. Totev. “Development of a controlled Vacuum Ultraviolet Light Source for the Characterization and Testing of Silicon Photomultipliers for nEXO”. MA thesis. McGill University, 2020.
- [22] nEXO Collaboration et al. *nEXO Pre-Conceptual Design Report*. 2018.
- [23] J. Schechter and J. W. F. Valle. “Neutrinoless double- β decay in $SU(2)\times U(1)$ theories”. In: *Physical Review D* 25 (11 1982), pp. 2951–2954.

- [24] Jun-Hao Liu, Jue Zhang, and Shun Zhou. “Majorana neutrino masses from neutrinoless double-beta decays and lepton-number-violating meson decays”. In: *Physics Letters B* 760 (2016), pp. 571–576.
- [25] Michelle J. Dolinski, Alan W.P. Poon, and Werner Rodejohann. “Neutrinoless Double-Beta Decay: Status and Prospects”. In: *Annual Review of Nuclear and Particle Science* 69.1 (2019), pp. 219–251.
- [26] M. Sajjad Athar et al. “Status and perspectives of neutrino physics”. In: *Progress in Particle and Nuclear Physics* 124 (2022), p. 103947.
- [27] A. S. Barabash et al. “Final results of the Aurora experiment to study 2β decay of ^{116}Cd with enriched $^{116}\text{CdWO}_4$ crystal scintillators”. In: *Physical Review D* 98.9 (2018).
- [28] D. Q. Adams et al. “Search for Majorana neutrinos exploiting millikelvin cryogenics with CUORE”. In: *Nature* 604.7904 (2022), pp. 53–58.
- [29] O. Azzolini et al. “Final Result of CUPID-0 Phase-I in the Search for the for the ^{82}Se Neutrinoless Double Beta Decay”. In: *Physical Review Letters* 123.3 (2019).
- [30] E. Armengaud et al. “New Limit for Neutrinoless Double-Beta Decay of ^{100}Mo from the CUPID-Mo Experiment”. In: *Physical Review Letters* 126.18 (2021).
- [31] S Umehara et al. “Double beta decay of ^{48}Ca studied by $\text{CaF}_2(\text{Eu})$ scintillators”. In: *Journal of Physics: Conference Series* 120.5 (2008), p. 052058.
- [32] G. Anton et al. “Search for Neutrinoless Double- β Decay with the Complete EXO-200 Dataset”. In: *Physical Review Letters* 123 (16 2019), p. 161802.
- [33] M. Agostini et al. “Final Results of GERDA on the Search for Neutrinoless Double- β Decay”. In: *Physical Review Letters* 125.25 (2020).
- [34] S. Abe et al. “Search for the Majorana Nature of Neutrinos in the Inverted Mass Ordering Region with KamLAND-Zen”. In: *Physical Review Letters* 130 (5 2023), p. 051801.

- [35] I. J. Arnquist et al. “Final Result of the Majorana Demonstrator’s Search for Neutrinoless Double- β Decay in ^{76}Ge ”. In: *Phys. Rev. Lett.* 130 (6 Feb. 2023), p. 062501.
- [36] R. Arnold et al. “Measurement of the $2\nu\beta\beta$ decay half-life of ^{150}Nd and a search for $0\nu\beta\beta$ decay processes with the full exposure from the NEMO-3 detector”. In: *Physical Review D* 94.7 (2016).
- [37] J. Argyriades et al. “Measurement of the two neutrino double beta decay half-life of Zr-96 with the NEMO-3 detector”. In: *Nuclear Physics A* 847.3-4 (2010), pp. 168–179.
- [38] E. Aprile and T. Doke. “Liquid xenon detectors for particle physics and astrophysics”. In: *Reviews of Modern Physics* 82.3 (2010), pp. 2053–2097.
- [39] J. B. Albert et al. “Improved measurement of the $2\nu\beta\beta$ half-life of Xe-136 with EXO-200”. In: *Physical Review C* 89.1 (2014).
- [40] M Auger et al. “The EXO-200 detector, part I: detector design and construction”. In: *Journal of Instrumentation* 7.05 (2012), P05010.
- [41] Juris Meija et al. “Isotopic compositions of the elements 2013 (IUPAC Technical Report)”. In: *Pure and Applied Chemistry* 88.3 (2016), pp. 293–306.
- [42] J.B. Albert et al. “Cosmogenic backgrounds to $0\nu\beta\beta$ in EXO-200”. In: *Journal of Cosmology and Astroparticle Physics* 2016.04 (2016), pp. 029–029.
- [43] R. Neilson et al. “Characterization of large area APDs for the EXO-200 detector”. In: *Nuclear Instruments and Methods in Physics Research Section A: Accelerators, Spectrometers, Detectors and Associated Equipment* 608.1 (2009), pp. 68–75.
- [44] E. Conti et al. “Correlated fluctuations between luminescence and ionization in liquid xenon”. In: *Physical Review B* 68 (5 2003), p. 054201.
- [45] J. B. Albert et al. “Investigation of radioactivity-induced backgrounds in EXO-200”. In: *Physical Review C* 92 (1 2015), p. 015503.

- [46] D.S. Leonard et al. “Trace radioactive impurities in final construction materials for EXO-200”. In: *Nuclear Instruments and Methods in Physics Research Section A: Accelerators, Spectrometers, Detectors and Associated Equipment* 871 (2017), pp. 169–179.
- [47] G. Gallina et al. “Performance of novel VUV-sensitive Silicon Photo-Multipliers for nEXO”. In: *European Physical Journal. C, Particles and Fields (Online)* 82.12 (2022).
- [48] SNOLAB. *User’s Handbook*. 2006.
- [49] T. Stiegler et al. “Event reconstruction in a liquid xenon Time Projection Chamber with an optically-open field cage”. In: *Nuclear Instruments and Methods in Physics Research Section A: Accelerators, Spectrometers, Detectors and Associated Equipment* 1000 (2021), p. 165239.
- [50] nEXO Collaboration. “Conceptual Design Report: Photon Detector”. Unpublished. Jan. 2023.
- [51] M. Jewell et al. “Characterization of an Ionization Readout Tile for nEXO”. In: *Journal of Instrumentation* 13.01 (2018), P01006.
- [52] Z. Li et al. “Simulation of charge readout with segmented tiles in nEXO”. In: *Journal of Instrumentation* 14.09 (2019), P09020–P09020.
- [53] D Renker and E Lorenz. “Advances in solid state photon detectors”. In: *Journal of Instrumentation* 4.04 (2009), P04004.
- [54] H.N. Becker and A.H. Johnston. “Dark current degradation of near infrared avalanche photodiodes from proton irradiation”. In: *IEEE Transactions on Nuclear Science* 51.6 (2004), pp. 3572–3578.
- [55] *What is an SiPM and how does it work?* URL: <https://hub.hamamatsu.com/us/en/technical-notes/mppc-sipms/what-is-an-SiPM-and-how-does-it-work.html>. (Accessed: 01.10.2022).

- [56] A. Vacheret et al. “Characterization and simulation of the response of Multi-Pixel Photon Counters to low light levels”. In: *Nuclear Instruments and Methods in Physics Research Section A: Accelerators, Spectrometers, Detectors and Associated Equipment* 656.1 (2011), pp. 69–83.
- [57] A. Jamil et al. “VUV-Sensitive Silicon Photomultipliers for Xenon Scintillation Light Detection in nEXO”. In: *IEEE Transactions on Nuclear Science* 65.11 (2018), pp. 2823–2833.
- [58] G. Gallina et al. “Characterization of the Hamamatsu VUV4 MPPCs for nEXO”. In: *Nuclear Instruments and Methods in Physics Research Section A: Accelerators, Spectrometers, Detectors and Associated Equipment* 940 (2019), pp. 371–379.
- [59] Fabio Acerbi et al. “NUV and VUV sensitive Silicon Photomultipliers technologies optimized for operation at cryogenic temperatures”. In: *Nuclear Instruments and Methods in Physics Research Section A: Accelerators, Spectrometers, Detectors and Associated Equipment* 1046 (2023), p. 167683.
- [60] J. Zhang et al. “Scintillation detectors with silicon photomultiplier readout in a dilution refrigerator at temperatures down to 0.2 K”. In: *Journal of Instrumentation* 17.06 (2022), p. 06024.
- [61] *VUV-MPPC 4th generation (VUV4): Product Flyer*. 2017.
- [62] L. Darroch. “An Environmental Test Stand for Large Area Testing of Silicon Photomultipliers”. MA thesis. McGill University, 2019. MSc thesis.
- [63] *MidasWiki: Main Page*. URL: https://daq00.triumf.ca/MidasWiki/index.php/Main_Page. (Accessed: 21.10.2022).
- [64] *Charge sensitive preamplifiers explained*. URL: <https://www.cremat.com/why-use-csps/>. (Accessed: 19.10.2022).
- [65] *Step Motor Wiring Diagram*. URL: <https://www.applied-motion.com/sites/default/files/StepMotorWiring-8-lead-striped.pdf>. (Accessed: 30.10.2022).

- [66] C. Gingras and L. Darroch. *ETS Stage Controller*. <https://github.com/Brunner-neutrino-lab/ets-stage-controller/tree/main/scripts>. 2023. Private repository.
- [67] *Phidget Support: Language - Python*. URL: https://www.phidgets.com/docs/Language_-_Python. (Accessed: 16.05.2023).
- [68] *ROOT: analyzing petabytes of data, scientifically*. URL: <https://root.cern/>. (Accessed: 30.10.2022).
- [69] *merci*. URL: <https://bitbucket.org/team-waveformers/merci/src/devel/>. (Accessed: 19.10.2022).
- [70] *The minimum spot a laser beam can be focused?* URL: <https://www.researchgate.net/post/The-minimum-spot-a-laser-beam-can-be-focused>. (Accessed: 14.07.2022).
- [71] A. Fitzgibbon, M. Pilu, and R.B. Fisher. “Direct least-squares fitting of ellipses”. In: *IEEE Transactions on Pattern Analysis and Machine Intelligence* 21.5 (1999), pp. 476–480.
- [72] *Detection of Outliers*. URL: <https://www.itl.nist.gov/div898/handbook/eda/section3/eda35h.htm>. (Accessed: 14.01.2023).
- [73] Patrick Eckert et al. “Characterisation studies of silicon photomultipliers”. In: *Nuclear Instruments and Methods in Physics Research Section A: Accelerators, Spectrometers, Detectors and Associated Equipment* 620.2 (2010), pp. 217–226.
- [74] R. Pestotnik et al. “Silicon photomultiplier as a position sensitive detector of Cherenkov photons”. In: *Nuclear Instruments and Methods in Physics Research Section A: Accelerators, Spectrometers, Detectors and Associated Equipment* 581.1 (2007), pp. 457–460.

- [75] Fabio Acerbi et al. “Characterization of Single-Photon Time Resolution: From Single SPAD to Silicon Photomultiplier”. In: *IEEE Transactions on Nuclear Science* 61.5 (2014), pp. 2678–2686.